

Laboratory water-window x-ray microscopy

MIKAEL KÖRDEL,^{1,6,†} AURÉLIE DEHLINGER,^{2,3,7,†} CHRISTIAN SEIM,^{2,3} ULRICH VOGT,¹
EMELIE FOGELQVIST,^{1,5} JONAS A. SELLBERG,¹ HOLGER STIEL,^{3,4} AND HANS M. HERTZ^{1,*} 

¹Department of Applied Physics, AlbaNova University Center, KTH Royal Institute of Technology, 106 91 Stockholm, Sweden

²Institut for Optics and Atomic Physics, Technical University of Berlin, Hardenbergstr. 36, 10623 Berlin, Germany

³Berlin Laboratory for Innovative X-ray Technologies (BLIX), Hardenbergstr. 36, 10623 Berlin, Germany

⁴Max-Born-Institute (MBI), Max-Born-Strasse 2A, 12489 Berlin, Germany

⁵Current address: Eclipse Optics, Vasagatan 52, 111 20 Stockholm, Sweden

⁶e-mail: mikael.kordel@biox.kth.se

⁷e-mail: a.dehlinger@tu-berlin.de

*Corresponding author: hertz@biox.kth.se

Received 23 March 2020; revised 4 May 2020; accepted 4 May 2020 (Doc. ID 393014); published 8 June 2020

Soft x-ray microscopy in the water window ($\sim 285\text{--}535$ eV) is an emerging and unique tool for 2D and 3D imaging of unstained intact cellular samples in their near-native state with few-10-nm detail. However, present microscopes rely on the high x-ray brightness of synchrotron-radiation sources. Having access to water-window microscopy in the home laboratory would increase the impact and extend the applicability of the method. In the present paper, we review three decades of efforts to build laboratory water-window microscopes and conclude that the method is now reaching the maturity to allow biological studies. The instruments as well as their key components are quantitatively and qualitatively compared. We find that the brightness and the reliability of the laboratory source are the most critical parameters, but that the optics as well as the sample preparation also must be optimized to enable high-resolution imaging with adequate exposure times. We then describe the two sister microscopes in Stockholm and Berlin, which allow reliable high-resolution biological imaging with short exposure times of a few tens of seconds in 2D and a few tens of minutes in 3D. They both rely on a liquid-jet laser-plasma source combined with high-reflectivity normal-incidence multilayer condenser optics, high-resolution zone-plate imaging optics, CCD detection, and cryogenic sample handling. Finally, we present several examples of biological imaging demonstrating the unique properties of these instruments. © 2020 Optical Society of America under the terms of the [OSA Open Access Publishing Agreement](https://doi.org/10.1364/OPTICA.393014)

<https://doi.org/10.1364/OPTICA.393014>

1. INTRODUCTION

Microscopy allows us to observe life processes that span the entire range from the single-molecule level to the cellular and tissue level. However, we still lack methods that allow 10-nm-range three-dimensional (3D) imaging in intact thick objects such as cells or tissue. Present high-resolution methods are typically limited to thin objects, small volumes, or processed samples, making it difficult to study nanometer detail in the context of the full undisturbed cell-biological system. Examples of such tools include electron and scanned-probe microscopes, which require thin samples or surfaces, respectively, and superresolution optical microscopes (STED, PALM, etc.), which have intrinsic difficulties providing full 3D imaging with reasonable exposure times.

X rays have the short wavelength and the appropriate absorption and scattering properties necessary for high-resolution imaging of thick objects. X-ray methods are therefore emerging as the prime candidate for 3D nano-imaging of intact unstained cells in their native or near-native state. The two major classes of imaging methods are lens-based soft x-ray microscopy (XRM) [1–4] and lensless hard x-ray coherent diffraction imaging (CDI)

[5]. CDI is the more recent method. It has a potential dose advantage by avoiding lenses and presently claims 25–50 nm half-period resolution on freeze-dried cells. XRM in the water window [1,3,4] demonstrates the same resolution but, importantly, on cryo-fixed hydrated cells, thereby allowing XRM to show many biological results of high relevance. Both methods are enabled by the high-brightness x-ray sources provided at large-scale facilities for synchrotron radiation or free-electron lasers, thereby limiting the accessibility to and use of the methods for biological scientists. Only soft x-ray microscopy has the potential to go laboratory scale. CDI requires much more coherent photon flux than present laboratory soft x-ray sources can provide.

Soft XRM in the water window ($\lambda \approx 2.3\text{--}4.3$ nm, $E \approx 285\text{--}535$ eV) allows high-resolution imaging of intact, thick hydrated samples with natural contrast. The basic idea is to use the large difference in absorption between carbon (e.g., proteins and lipids) and oxygen (e.g., water) in the water window. The use of this short wavelength also has the advantage that diffraction in principle allows for 2–4 nm resolution. In addition to the work with natural contrast, biochemical sensitivity and selectivity

may be obtained with protein-specific x-ray-sensitive probes. In the last couple of years, 3D soft x-ray microscopy of cryo-fixed cells (“x-ray cryo-tomography”) has emerged and is now delivering unique results on a wide range of biologically relevant topics [6–9]. As in electron microscopy, cryogenic sample preparation is essential for mitigating dose damage. In addition to providing 3D images of intact hydrated cells in their near-native state, x-ray cryo-tomography allows classification of different intracellular structures (e.g., lipid droplets, mitochondria, nuclei, vacuoles) due to quantitative determination of the local absorption coefficient via Beer–Lambert’s law, in analogy to the macroscopic x-ray imaging of computed tomography (CT). These results have all been obtained at the (few) soft x-ray microscopes presently available at synchrotron-radiation facilities. However, many biological researchers would benefit from having everyday access to an x-ray microscope in their home laboratories.

After several years of research and development, laboratory water-window x-ray microscopes are now reaching maturity [10,11]. The major advantages of a laboratory-scale microscope compared to a synchrotron-based instrument are 1) easier integration with any complementary methods in the home laboratory; 2) increased access for a wider user community; and 3) unlimited “beam time,” therefore allowing the often time-consuming but crucial iterative optimization of sample preparation techniques for each biological task under investigation. In the present paper, we will first review the field of laboratory soft x-ray microscopy for cell-biological applications, then discuss the design of two state-of-the-art laboratory microscopes, and finally give several examples of unique biological imaging with these instruments.

2. LABORATORY SOFT X-RAY MICROSCOPES

A. Contact XRM

Soft x-ray contact microscopy was first developed at the IBM T. J. Watson Research Center [12]. While the early experiments relied on a synchrotron-radiation source, the development of laser-plasma sources soon allowed this technique to be performed in the laboratory [13,14]. In contact microscopy, the specimen is placed directly on or in close proximity to a high-resolution x-ray sensitive resist (e.g., PMMA) and is then irradiated by soft x-rays. The exposed resist is subsequently developed so that its resulting topography reveals the specimen’s absorbance. This 1:1 image of the specimen can be detected by high-resolution methods, e.g., scanning electron microscopy or atomic force microscopy. In recent years, laboratory contact microscopy has been conducted at the Military University of Technology in Warsaw [15], the Japan Atomic Energy Research Agency in Kyoto [16], and the Institute of Multidisciplinary Research for Advanced Materials in Sendai [17].

Soft x-ray contact microscopy has the principal advantage of allowing short single-pulse exposures with high-power laser plasmas, thereby avoiding the radiation-dose issues that come with imaging at noncryogenic temperatures. However, the spatial resolution and image quality is typically limited by diffraction and penumbral blur due to the finite sample thickness and sample-to-resist distance as well as by nonlinear effects in the resist development [18–20]. These limitations, together with the time-consuming readout, have hindered the method from producing results of biological relevance.

B. Scanning XRM

Scanning transmission XRM (STXM) was pioneered by Kirz and coworkers at Stony Brook and first demonstrated at a synchrotron radiation source [21]. In the original STXM, a zone-plate-focused soft x-ray beam is scanned over the sample, sequentially recording the transmission at each pixel. In recent years, this powerful principle has been extended to recording, e.g., x-ray fluorescence for determining elemental composition orptychography for sub-x-ray spot-size resolution imaging. The method is extensively used at synchrotron-radiation facilities, where both high photon flux and high coherence are available (e.g., Elettra [22], ALS [23], CLS [24], ESRF [25], APS [26], PETRA III [27]).

Unfortunately, laboratory soft x-ray sources do not have the brightness to allow scanning soft XRM with acceptable acquisition times in the home laboratory. In Ref. [28], the potential of laser-produced plasma sources for STXM was investigated. Subsequently, a few proof-of-principle experiments with tabletop scanning soft x-ray microscopes were published [29,30] in the 1990s, but no attempts have been reported since.

C. Full-Field XRM

Full-field transmission soft XRM (TXM) was pioneered by Schmahl and coworkers in Göttingen and first demonstrated at synchrotron-radiation facilities [31]. The basic TXM arrangement resembles that of a conventional visible-light microscope, i.e., a condenser illuminates the object and a high-resolution zone-plate optic produces a magnified absorption-contrast image on the detector. Contrary to the visible-light microscope, the sample can be mounted on a rotational stage to enable tomographic 3D imaging by recording several angular projections. Key enablers for recent high-resolution biological imaging [3,4,6–9,32–34] are high-quality x-ray optics and cryogenic sample preparation to avoid radiation damage. State-of-the-art synchrotron-based full-field water-window TXMs are in operation at ALS/Berkeley [3,35], HZB/Berlin [4,36], and ALBA/Barcelona [7,37].

The first attempt to build a laboratory soft x-ray microscope was also made by Schmahl and coworkers in 1992 [38]. The general x-ray optical arrangement is the same as for the synchrotron microscope, and the key issue is finding a sufficiently bright and reliable laboratory x-ray source. This first laboratory microscope was based on a nitrogen-gas discharge plasma source [39], providing line emission suitable for diffractive zone-plate high-resolution optics. To date, soft XRM based on different types of discharge sources has been demonstrated by the Institute for Laser Technology (ILT) in Aachen [40] and by Energetiq, in Massachusetts [41]. The discharge plasma sources are attractive due to their compactness, stability, reliability, and large flux. Unfortunately, present discharge sources typically produce a large source size, resulting in a limited x-ray brightness. Thus, x-ray microscopes using these sources have so far had difficulty reaching an observable resolution significantly better than that of a visible-light microscope when operated at acceptable exposure times. Soft XRM with higher resolution requires a brighter source.

The first laboratory soft x-ray transmission microscope with subvisible resolution was demonstrated by Hertz and coworkers at the Royal Institute of Technology (KTH) in Stockholm in 2000 [10]. It was based on a liquid-jet high-brightness laser-plasma source providing a regenerative target and narrow-bandwidth line emission in combination with a multilayer condenser mirror

and zone-plate optics. This microscope design has since evolved and now includes a higher-power laser as well as cryogenic and tomographic sample handling, enabling short-exposure biological imaging with high resolution [11]. A sister microscope based on the same principles was designed by Stiel and coworkers and is now operated at the Berlin Laboratory for Innovative X-Ray Technologies (BLiX) at the Technical University (TU) of Berlin [42]. These two microscopes have demonstrated imaging with early synchrotron-like quality and acceptable exposure times, allowing unique and relevant biological imaging. They are described in more detail in Section 4.

Several other groups have demonstrated soft XRM using different types of laser-plasma sources. This includes systems based on regenerative gas-puff laser plasmas (Military University of Technology (MUT) in Warsaw [43] and Laser-Laboratorium Göttingen [44]), solid-metal target laser plasmas (Tsukuba [45] and SiriusXT in Dublin [46]), and liquid-jet laser plasmas (Wonkwang in Korea [47]). In addition, we note an attempt to build a microscope based on an electron-impact source (University of Tokyo) [48]. Several of these instruments have potential but have not yet demonstrated high-resolution biological imaging, primarily since the present source performance is insufficient. With improved source brightness, these designs, just as with the discharge-based microscopes, may become interesting alternatives.

3. LABORATORY FULL-FIELD WATER-WINDOW MICROSCOPES

A. Introduction

The general arrangement of a laboratory full-field soft x-ray microscope is depicted in Fig. 1. It consists of an x-ray source, condenser optics, a high-resolution imaging objective, and an x-ray detector. The condenser, which collects the emission from the source to illuminate the sample, can either be positioned between the source and the sample, as shown in Fig. 1, or behind the source. The latter would be the arrangement used with a normal-incidence condenser mirror. In either case, a central stop must be placed between the source and the sample to block direct light from the source flooding the detector. This results in the characteristic hollow-cone illumination. The inset in Fig. 1 depicts the water window and its natural carbon/oxygen contrast, indicating the advantage of operating the microscope at around 500 eV for maximum transmission through typical cell-biological samples.

The major difference between synchrotron-based soft x-ray microscopes and laboratory soft x-ray microscopes is the lower

brightness of the laboratory x-ray sources, making it difficult to obtain high spatial-resolution laboratory imaging with acceptable exposure times. Thus, when designing a laboratory microscope, a bright source is essential, but is still not sufficient on its own. In addition, it is necessary to ensure that every component in the rest of the system as well as the overall system design is as photon-efficient as possible. In the next few sections, we quantitatively and qualitatively discuss the key components of the full-field transmission water-window x-ray microscope.

B. Sources

The x-ray source is the most crucial component in the x-ray microscope. Essentially, the source has to deliver a sufficient number of x-ray photons per unit time, from a sufficiently small area, and with a suitable spectral bandwidth. In this respect, all available laboratory water-window sources are inferior to synchrotron-radiation sources. Figure 2 summarizes the principles of operation of the different types of laboratory sources used for TXM.

The figure of merit commonly used to compare x-ray sources is the spectral brightness, sometimes called *brilliance* or *brightness* for short, defined as photons/(s × sr × μm² × 0.1%BW). We note that this figure of merit is relevant in the sense that it describes the intensity of photons that can be used for imaging. A higher illumination intensity gives shorter exposure times, which is key to useful operation and the limiting factor in many laboratory x-ray microscopes. On the other hand, a larger solid angle of emission or a larger source area (both resulting in lower brightness) is not always a disadvantage in TXM. Nevertheless, comparison of the spectral brightness can provide a general overview and a good starting point for a more detailed discussion. Figure 3 compares the spectral brightness of laboratory as well as synchrotron sources [49,50].

1. Discharge Sources

The principle of discharge x-ray sources is to generate a hot plasma by driving a high-current pulse through a low-pressure gaseous target [cf. Fig. 2(e)]. The gas is injected into the gap between an anode and a cathode, where the plasma is ignited [51], or into an electrodeless, inductively coupled setup [52]. The plasma is initially formed with a density and temperature that is too low to produce considerable emission in the x-ray regime, but the free charges quickly induce a strong magnetic field that pulls the plasma toward the central axis [53]. The plasma is thereby compressed, and the temperature is increased. This process is known as *Z* pinch,

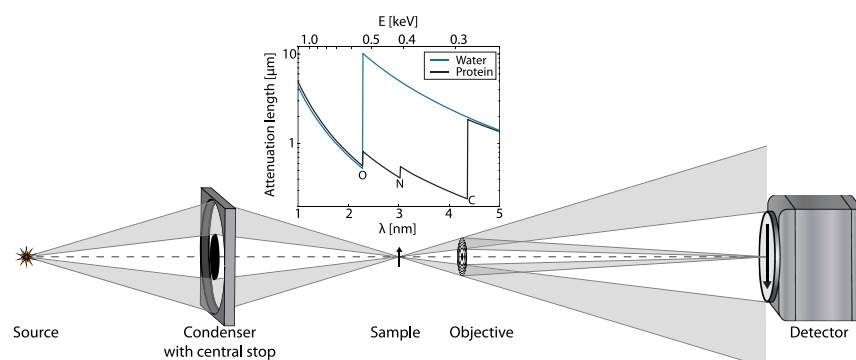


Fig. 1. Schematic arrangement of a transmission x-ray microscope with its most important components: source, condenser, sample, high-resolution objective, and detector. The inset depicts the water-window contrast mechanism.

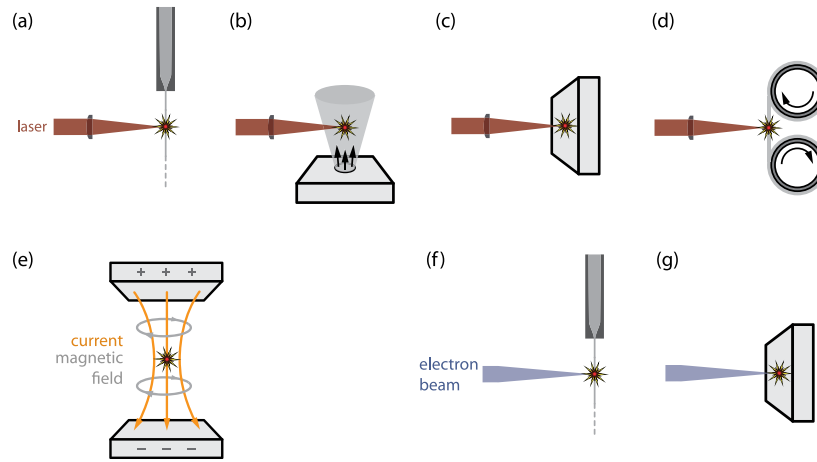


Fig. 2. Experimental arrangement of the major types of laboratory soft x-ray sources used for water-window microscopy. Laser plasma with (a) liquid-jet target, (b) gas-puff target, (c) solid target, (d) tape target, (e) pinch-plasma discharge source; electron-impact source with (f) liquid-jet target and (g) solid target.

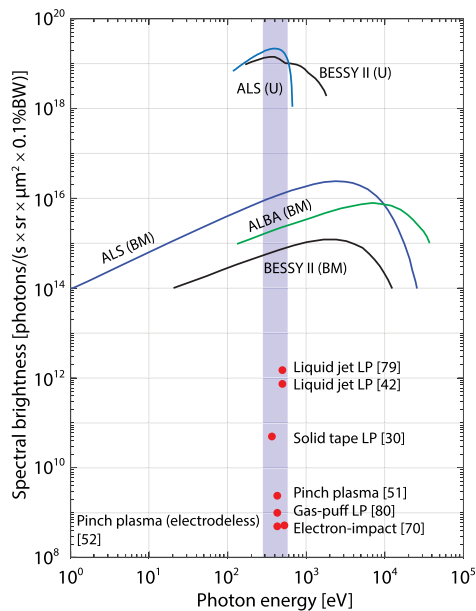


Fig. 3. Brightness of water-window laboratory sources used for microscopy (LP, laser plasma). The water-window energy range is indicated by the blue bar. For comparison, microscopy beamlines at three synchrotrons are included (U, undulator; BM, bending magnet).

and sources of this kind are referred to as pinch-plasma sources [51,54]. In addition, pseudo-spark geometries, using a hollow cathode (or anode), can help to compress the plasma and thereby achieve the desired emission [51,55].

The properties of x-ray emission can be partly explained by considering blackbody radiation and Wien's displacement law,

$$\lambda_{\text{peak}} = \frac{2.898 \cdot 10^6 \text{ nm} \cdot \text{K}}{T}. \quad (1)$$

It tells us that x-rays in the water window are emitted at temperatures of $\sim 10^6$ K. The total emission spectrum will consist of broadband bremsstrahlung emission combined with element-specific emission lines corresponding to discrete electronic

transitions. In the ideal case, the peak wavelength given by Wien's displacement law overlaps with the desired emission lines.

Discharge sources are currently used for x-ray generation in the water window [40,41]. They have also been used as sources for UV and extreme-UV (EUV) lithography, even though the laser-plasma sources have lately taken over much of this market [56,57].

2. Laser-Plasma Sources

Laser plasmas are created by focusing a high-power pulsed laser onto a target material. The incident laser light undergoes dissipative absorption, thereby thermally heating the material to form a plasma. The free electrons then continue to absorb energy by inverse bremsstrahlung, increasing the plasma temperature. As the laser light, of wavelength λ , propagates into the material the electron density increases until it reaches the critical density [58],

$$n_c = \frac{1.11 \cdot 10^9 \text{ } \mu\text{m}^{-1}}{\lambda^2}, \quad (2)$$

where the wave can no longer propagate and is instead reflected back and lost. Close to the critical electron density, the energy transfer is the most efficient, and consequently, a region of intense x-ray emission is created [58].

The basic properties of the x-ray emission from laser plasmas can be understood following the discussion for the discharge plasmas above. The peak wavelength according to Wien's displacement law should ideally coincide with the characteristic emission lines of the target material. Strong emission in the water window is obtained at plasma temperatures of $\sim 10^6$ K. It has been shown that the x-ray conversion efficiency of solid Au target laser plasmas is a few tens of percent for $\lambda = 1.06 \text{ } \mu\text{m}$ Nd lasers, and somewhat higher for the second- (0.53 μm) and fourth- (0.26 μm) harmonics [59]. By considering an equilibrium between incident and outgoing radiation, using the approximate conversion efficiency and the Stefan-Boltzmann law, it can be shown that laser intensities of approximately 10^{14} W/cm^2 are suitable for this application.

Laser-plasma sources used for XRM in the water window have utilized a wide range of target materials and target delivery methods. Figures 2(a)–2(d) depicts the major types, solid bulk [16,45,60,61], solid tape [30], liquid jet [62–65], and gas-puff

targets [66]. There is an obvious benefit of having a regenerative target, such as a liquid or a gas, since each laser pulse destroys the material. A continuous liquid jet typically operates with velocities of 20–50 m/s [67], providing new target material at a rate that allows for laser repetition rates up to several kilohertz, which translates to high average x-ray power and brightness. Gas targets typically operate with discrete gas puffs, which requires synchronization with the laser [43] as well as evacuation of the gas between pulses. The latter will effectively limit the repetition rate of the laser to around 10 Hz.

3. Electron-Impact Sources

Conventional electron-impact x-ray sources have been developed for the water window and are based either on solid targets, with a high oxygen content, such as metal oxides [48,68] or liquid water jets [69,70] [cf. Figs. 2(f)–2(g)]. These sources emit oxygen K_α photons by the interaction of a high-power electron beam with the target material. However, it should also be noted that secondary Auger decay will absorb a considerable part of the incident energy, especially for low- Z elements [68]. Since the photon energy of the oxygen K_α line is located at 525 eV, the effective penetration depth of the radiation in biological material is comparable to the corresponding values of laser-plasma and pinch-plasma sources operating with nitrogen as a target material.

4. Coherent Laboratory Sources

Due to their good beam properties, coherent x-ray sources, such as high harmonics generation (HHG) [71,72], plasma-based x-ray lasers (XRLs) [73,74], or betatron radiation produced by laser-wakefield accelerators (LWFAs) [75] initially emerged as promising candidates for laboratory XRM. The brightness of these sources covers a broad range [76] from 10^6 photons/(s \times sr \times $\mu\text{m}^2 \times 0.1\% \text{BW}$) up to 10^{15} photons/(s \times sr \times $\mu\text{m}^2 \times 0.1\% \text{BW}$), depending on the operating principle, the pump laser, and the target material. Although the performance of these sources has already been demonstrated for XRM in the EUV [76,77] and hard x-ray [78] regions, the application to water-window microscopy is mainly hindered by low flux (HHG) and huge and expensive pump lasers (XRL, LWFA). The brightness of HHG sources at the oxygen K edge could be increased once high-repetition rate mid-IR lasers become available. However, due to the high spatial coherence, these sources are better suited for techniques other than transmission x-ray microscopes, like CDI, ptychography, etc. For this reason, the coherent laboratory sources will not be further discussed here.

5. Comparison and Evaluation

Figure 3 summarizes the average spectral brightness of x-ray sources developed for laboratory XRM in the water window. For comparison, synchrotron sources based on undulator (U) and bending magnet (BM) radiation are included. We note that the liquid-jet laser plasmas stick out among the laboratory sources with around 10^{12} photons/(s \times sr \times $\mu\text{m}^2 \times 0.1\% \text{BW}$) [79], approaching the brightness of early BMs. Pinch plasmas and gas-puff laser plasmas present numbers that are more than 2 orders of magnitude lower (5×10^8 – 2.4×10^9 photons/(s \times sr \times $\mu\text{m}^2 \times 0.1\% \text{BW}$))

[40,52,80]. For pinch-plasma sources, the reason for this is primarily the size of the source. Even though stable operation is achieved at high power, the source diameter is typically 400 μm [51], which can be compared to a typical liquid-jet laser plasma of 20 μm [79]. The pinch plasmas can reach electron densities in the range of $n_e = 10^{20}$ cm^{-3} at electron temperatures of $> 10^6$ K [54]. This can be compared to the critical electron density in a laser plasma, where the laser can no longer penetrate the target, which is $n_e \approx 10^{21}$ cm^{-3} (Eq. 2) for a 1064 nm wavelength Nd:YAG laser. The gas-puff laser plasma is also typically larger [81] and of lower density than the liquid-jet laser plasma, resulting in significantly lower brightness. Furthermore, due to thermal and vacuum restrictions, the operation frequency of the gas-puff nozzle is limited to 10 Hz (or below), making it challenging to scale this source to high average photon fluxes in its present implementation.

To our knowledge, there are no recent quantitative measurements of the water-window brightness of solid-target laser-plasma sources, even though they are currently being developed and evaluated [61]. One example using a 20 μm thick, 4 mm wide Mylar tape as a target measured a brightness of about 5×10^{10} photons/(s \times sr \times $\mu\text{m}^2 \times 0.1\% \text{BW}$), resulting in noisy images acquired in scanning mode [30,82].

In addition to brightness, the debris emission is of critical importance for all plasma sources. Such debris deposits and destroys surrounding components, e.g., optics. Sensitive optics in the vicinity of the source may include condenser optics, like zone plates or mirrors, shutters, vacuum windows, filters, and even the source components. Solid-target laser plasmas are known to produce significant amounts of debris. Thus, these systems are difficult to operate in microscope systems for extended periods. Very low-debris operation is reported from gas-puff laser plasmas using nitrogen as target material [83]. Also, the liquid-jet laser plasmas have reported negligible debris operation [63,64,84]. Here, the plasma needs to be operated far away from the nozzle (> 3 mm) to avoid destroying it, setting high demands on the jet stability [67]. Similarly, electrode erosion in discharge plasma sources is a serious problem, limiting the average input power for continuous operation [51].

The compact electron-impact source used for water-window microscopy, described by Ohsuka *et al.* [48], exhibits a brightness of about 10^4 photons/(s \times sr \times $\mu\text{m}^2 \times \text{line}$), several orders of magnitude below the brightness of laser-plasma or pinch-plasma sources. A high-brightness water-window electron-impact source based on a liquid water jet is described in [70]. It relies on an 8 W electron gun resulting in a brightness of 5×10^8 photons/(s \times sr \times $\mu\text{m}^2 \times 0.1\% \text{BW}$), which is the number included in Fig. 3. The authors stated that by using an electron gun with a power > 200 W, the brightness could be increased by at least 1 order of magnitude. The main drawbacks of electron-impact sources, besides the low brightness, are the thermal stability of the target as well as the lifetime of the (high-power) electron gun in a gaseous environment.

C. X-Ray Optics

In the soft x-ray range, the index of refraction of materials is very close to 1, and the absorption of radiation in materials is very high. Therefore, refractive lenses known from visible-light microscopes cannot be used, and alternative optics based on reflection or diffraction are the only options. Nevertheless, the optical concept of a full-field water-window laboratory x-ray microscope is very

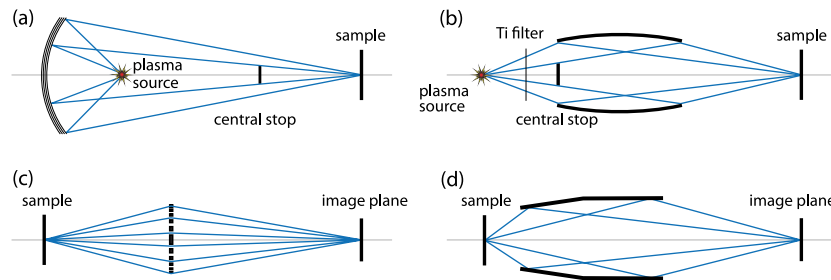


Fig. 4. X-ray optics overview. Upper row depicts condenser arrangements based on (a) normal-incidence multilayer optics and (b) grazing-incidence optics. Lower row shows high-resolution imaging with (c) zone-plate optics and (d) Wolter optics.

similar to the one of a visible-light microscope and consists of a condenser to illuminate the sample and an objective to create a magnified image on a detector. We can therefore rely on the principles of the optical microscope when designing the x-ray optical system of a laboratory soft x-ray microscope but with one important constraint: Given the limited numbers of photons from the laboratory sources, the efficiency of the optical components and the system as a whole is of key importance for acceptable microscope operation. Figure 4 summarizes the principles of the optical components used in laboratory water-window microscopy.

1. Condenser Optics

The role of the condenser is to collect as much light as possible from the source and illuminate the sample. The classical Köhler layout [85] consists of two lenses to achieve uniform illumination. For soft x-rays, this design is not possible, and instead critical illumination is employed, where the source is imaged directly onto the sample. This results in a nonuniform illumination of the object, with a source image slightly larger than the field of view. Another important aspect is partially coherent illumination in order to obtain the best possible resolution. The common choice is to match the numerical aperture (NA) of the condenser to the NA of the objective, which results in a resolution corresponding to the Rayleigh criterion for incoherent point sources. However, slightly better resolution can be achieved when the NA of the condenser is slightly larger (e.g., ~ 1.5 times) than the NA of the objective [85].

Multilayer mirrors: The use of a simple spherical mirror in normal incidence is a convenient condenser arrangement. However, the reflectivity of a single-material mirror for soft x-rays in normal incidence is very low, because the refractive index is close to 1. A solution is given by multilayer mirrors [86]. They usually consist of two materials that are periodically deposited onto one another. To reduce diffusion effects between the individual layers, it is sometimes necessary to add a third barrier layer. If the period of the layers satisfies Bragg's law, i.e., half the wavelength for normal incidence, the multiple interfaces backscatter the incident radiation in phase, thus greatly increasing the mirror's reflectivity. The bandwidth of the reflected radiation is given by the number of layer pairs, so that the mirror acts as a spectral filter, which is important when objective optics are chromatic, such as zone plates.

The production of high-reflectivity normal-incidence soft x-ray multilayers in the water window is very challenging, since it requires precise deposition of smooth subnanometer material layers. Fabricating condenser mirrors is particularly difficult, since deposition must be uniform over large areas with a very exact layer spacing that matches the wavelength of the line-emitting sources.

Early mirrors made from W/B_4C and Cr/Sc had a reflectivity of around 0.5% and 3%, respectively, and were used to build successful laboratory water-window x-ray microscopes at $\lambda = 3.37$ nm [10,87]. The latest generation soft x-ray multilayer condensers in normal incidence are made by magnetron sputtering in Cr/V , reaching an impressive average reflectivity over the ~ 50 mm diameter mirrors of 4%–5% for $\lambda = 2.48$ nm [11,88,89]. The radius of curvature and distances are chosen so that the condenser NA approximately matches the NA of objective optics ($NA \sim 0.05$). The bandwidth is $E/\Delta E \sim 400$.

Grazing-incidence mirrors: An alternative to multilayer mirrors is grazing-incidence optics, which are based on total external reflection [86]. A reflectivity $>75\%$ can theoretically be achieved for incidence angles smaller than the critical angle, assuming error-free metal mirrors. The simplest shape for imaging a point source into another point is an ellipse [86]. Accordingly, some laboratory water-window x-ray microscopes have used ellipsoidal condenser mirrors with a Ni-coated mirror surface [40,41,44,47,83]. These mirrors operate at grazing-incidence angles of few degrees (typically 1–3°) and have a calculated reflectivity between 40%–70%, depending on the mirror surface roughness, incidence angle, and other factors [90]. Thus, the NA of the elliptical condenser is very similar to the NA of the multilayer condenser.

Ellipsoidal mirrors typically suffer from figure errors and large off-axis aberrations, which means that the image of the source will be far from perfect. This might actually help to ensure a uniform illumination of the field of view, but can also considerably decrease the number of photons available for imaging with the objective. A possible solution to the aberration problem is the so-called Wolter mirror (Type I), which consists of two mirror surfaces, parabolic and hyperbolic [86]. Such a mirror can produce a high-quality image of the source onto the sample, but the fabrication of a Wolter mirror is much more difficult than fabrication of an elliptical mirror. Moreover, a Wolter condenser uses two reflections instead of one, which reduces the number of reflected photons. Nevertheless, laboratory water-window x-ray microscopes with Wolter mirror condensers have been demonstrated [45,48,60].

Zone plates: Zone plates are diffractive optics and will be described in more detail in the next section. A zone plate was used as condenser optic in an early laboratory microscope [91], but was soon replaced by a multilayer mirror condenser. The reason was the difficulty in achieving aperture-matched conditions, which led to a decreased resolution and introduced coherence artifacts [92].

2. Comparison and Evaluation of Condenser Optics

The two most common condenser concepts in laboratory water-window microscopy are multilayer mirrors and ellipsoidal mirrors. Both condensers use critical illumination with aperture matching to the objective, with a typical NA of approximately 0.05. In both cases, a central stop is necessary to block direct illumination from the source. The collected solid angles of the incident radiation are comparable. The reflectivity of the elliptical mirror in grazing incidence is much larger than that of the multilayer in normal incidence. However, off-axis aberrations and figure errors from an elliptical mirror can smear photons in the object plane outside the field of view, making it challenging to use these condensers with small high-brightness sources like laser plasmas.

A main difference between the grazing-incidence optics and multilayer optics is their reflectivity bandwidth. A multilayer mirror has a small bandwidth and therefore acts as a monochromator, selecting a specific line from the source spectrum. This is advantageous when using objective optics with chromatic aberrations such as zone plates. A mirror in grazing incidence is an achromatic optic and has to be used in combination with a spectral filter if the objective requires a small bandwidth. A more practical aspect is the condenser alignment procedure. A normal-incidence multilayer mirror is, due to its spherical shape and the on-axis optical arrangement, quite easy to align. In comparison, an ellipsoidal mirror can be very difficult to align due to its sensitivity to minor alignment errors, especially if the source is small.

A more uncommon condenser is the Wolter mirror, which combines grazing incidence conditions with good imaging characteristics. Both ellipsoidal and multilayer mirrors are commercially available, which is not the case for the Wolter mirror.

3. Objective Optics

The objective optic is generally the most important part of a microscope, since it determines the spatial resolution that can be obtained. For a condenser illumination that has the same NA as the objective, the smallest period (d) that can be resolved is given by [86]

$$d = \frac{0.61\lambda}{\text{NA}} = \Delta_{\text{Rayl}}. \quad (3)$$

This is equal to the well-known Rayleigh resolution limit Δ_{Rayl} , which defines the smallest observable distance between two point emitters. For visible light, NAs close to unity are common, and the resolution is ultimately limited by the wavelength λ . This is not the case for soft x-ray optics due to much smaller NAs, so the resolvable detail of water-window x-ray microscopes is often an order of magnitude larger than the wavelength, as explained in the next paragraph.

Zone plates: The most common objectives are zone plates, which have a long tradition in XRM. Zone plates are circular diffraction gratings with radially decreasing zone widths. Already in 1952, Kirkpatrick suggested that zone plates are well-suited objective optics for soft XRM [93]. The XRM group in Göttingen was the first to produce and include zone-plate objectives in both their laboratory and synchrotron-based microscopy arrangements [94]. The most important optical characteristics of zone plates are resolution and efficiency. The resolution of a zone plate according to Eq. (3) is given by

$$\Delta_{\text{Rayl}} = 1.22\Delta r, \quad (4)$$

where Δr is the width of the outermost zone. This means that for highest resolution, the outermost zone should be as small as possible. Since x-ray zone plates are binary structures, they have many diffraction orders and normally only the first order is used for imaging. The efficiency is defined as the number of photons incident on the zone plate divided by the photons in the first diffraction order. An efficiency maximum for soft x-rays is obtained when the thickness of the zones results in a phase shift close to π of the incoming radiation. High efficiency is especially important in laboratory-source-based microscopy.

Nowadays, fabrication of zone plates is exclusively done by electron beam lithography [86]. Consecutive nanofabrication steps typically include dry etching and electroplating. The preferred zone-plate material for water-window x-rays is Ni, due to well-established electroplating processes in combination with good x-ray optical characteristics. Theoretically, optimal efficiencies of about 20% are reached for zone thicknesses around 200 nm. This thickness can be achieved for outermost zone widths of 20–30 nm. Due to fabrication errors, efficiencies of real Ni zone plates are typically up to 10%–15%. Zone plates made of Au are also an alternative, although they have slightly lower efficiency.

We finally note two more important zone-plate characteristics. The focal length of a zone plate is given by $f = D\Delta r/\lambda$, with D being the diameter of the optic. With a typical diameter of 100 μm , soft x-ray zone plates have relatively short focal lengths, resulting in working distances of around 1 mm. Moreover, since the focal length is wavelength-dependent, zone plates are chromatic optics and cannot be used with broadband illumination. The acceptable spectral monochromaticity $\lambda/\Delta\lambda$ is equal to the number of zones [86] and is typically between 500 and 1000.

Wolter mirrors: There have also been attempts to use Wolter Type I optics as objectives for laboratory water-window x-ray microscopes [45,48,60]. If combined with a Wolter mirror condenser, the obvious advantage would be the possibility of using a source with a broadband spectrum. However, the demonstrated spatial resolution is lower than for zone plates.

4. Comparison and Evaluation of Objective Optics

Zone plates are, in most cases, the primary choice as objectives. They offer high resolution, typically 20–30 nm, and are available from both commercial and academic suppliers. Although fragile, they are easy to work with and require only simple alignment. We note that zone plates with outermost zone widths below 10 nm have been demonstrated [95], which would enable even higher resolution. Unfortunately, the number of photons for constant signal-to-noise ratio in the image scales with the feature size to the power of 3. This directly leads to a considerable increase in exposure times, and experiments become impractical if the brightness of the source is limited. Further, the number of zones in a 10-nm zone plate at reasonable diameters would put extreme demands on the monochromaticity of the source. These are the reasons why 2D imaging of laboratory water-window x-ray microscopes is currently limited to a practical resolution of a 20 nm half-period, approximately an order of magnitude larger than the wavelength. Also, in 3D tomographic imaging, 30–40 nm zone plates are preferable, since the depth of focus (DOF) better matches typical cell-size objects (cf. Section 3.G).

D. Detector

Given the low efficiency of the x-ray optics and the limited brightness of the laboratory sources, it is fortunate that soft x-ray detection can be performed with high efficiency. The detector of choice in laboratory soft XRM is a cooled back-illuminated charge-coupled device (CCD). Scientific-grade CCDs provide high sensitivity, excellent linearity, low noise characteristics, and a high number of pixels in combination with high dynamic range [96]. The alternative, complementary metal-oxide-semiconductor (CMOS) sensors, has the advantage of faster readout at the price of smaller dynamic range and higher noise. Typically, for the photon flux available in laboratory microscopes, the lower noise of the CCD is more important than the faster readout of the CMOS.

The CCD was first demonstrated by Smith and Boyle [97,98]. The pixels of a CCD detector are composed of p-doped metal-oxide-semiconductor (MOS) capacitors—usually p-Si with an optically transparent SiO₂ isolator layer with electrodes (so-called gates) on top and channel stops to separate and to read out the pixels. When a positive voltage is applied to a gate electrode, a potential well forms in the p-doped semiconductor in which the electrons from electron-hole pairs created by incoming x-ray photons are collected and accumulated. This electric charge is proportional to the number of incoming photons if the pixel is read out before its maximum full well capacity is reached. CCDs for soft x-rays [99] are illuminated from the back, since otherwise soft x-rays would be—in contrast to visible light—absorbed completely by the SiO₂ isolator layer and the gate electrodes before entering the p-doped semiconductor. The number of electrons generated by incoming photons with a specific energy defines the sensor's quantum efficiency, which is a crucial property for low photon-flux applications.

The readout of a CCD is realized by applying a control circuit to clock the pixels, so that their charge packets are transferred directionally to the neighboring pixel. This transfer goes on from pixel to pixel until the last one is reached, from which the electrons then reach a charge amplifier and are subsequently converted into a voltage, one pixel after another. As the amplification is carried out by the same external amplifier (with lower amplifier noise than in a CMOS) for all pixels, a high reproducibility between the pixels is achieved, directly resulting in a high linearity of the sensor. The digitization of the signal in scientific-grade CCD sensors is usually carried out in a 16-bit or 18-bit external analog-to-digital converter (low quantization noise).

The sensor of choice in laboratory soft XRM is typically a cooled back-illuminated 16-bit CCD with a pixel size of 13.5 μm and 4 megapixels (2048 pixels × 2048 pixels). It exhibits high quantum efficiency, up to 85% at 500 eV photon energy, in combination with low dark current noise, down to 0.001 electrons/photons/s at −70 °C [100]. At magnifications of 1000×, this results in an effective pixel size of 13.5 nm. If the microscope operates at lower magnifications, undersampling can cause the images to show lower resolutions than the optical capability of the microscope.

E. Sample Environment and Sample Preparation

For any imaging technique, it is of crucial importance that the sample be treated so that its properties are intact throughout the entire imaging procedure. Here, a major advantage of XRM is the limited need for sample preparation compared to other high-resolution techniques like, e.g., transmission electron microscopy (TEM).

X-ray microscopy relies on the natural difference in absorption between elements, in this case, the carbon/oxygen contrast in the water window (cf. Fig. 1, inset). Thereby, chemical staining is unnecessary, and the sample can be kept in a native or near-native environment. Furthermore, the absorption and scattering properties of x-rays allow imaging of samples that are several micrometers thick, which eliminates the need for sectioning. Still, for wet and cryogenic x-ray imaging, care must be taken to keep the sample water layer thin in order to avoid unnecessary loss of photons in the photon-limited laboratory x-ray microscope.

1. Dry Samples

Dry samples have been imaged with synchrotron-based x-ray microscopes for several decades [31] and with laboratory-based x-ray microscopes for a few decades [38]. Examples include diatoms, nanoparticles, and test targets, such as Siemens stars. These are typically placed on 20–50 nm thick silicon nitride (Si₃N₄) window grids, also commonly used in TEM. For this kind of imaging, the samples do not need any further fixation, and the preparation is often uncomplicated.

Laboratory XRM has also been applied to dehydrated cell samples [83,91]. This is, however, not the preferred preparation of biological specimens, for two reasons: the dehydration process will alter the morphology of most specimens and most biological specimens are very sensitive to radiation damage. Both can be avoided by cryo-freezing the sample. This is discussed in more detail in Section 3.E.4.

2. Chemically Fixed Samples

There are various chemical methods to fixate cell samples prior to imaging [101,102]. This is not commonly used in XRM, since the extent of the effects that the chemicals have on the samples is not fully understood. Ref. [101] investigated the effects of glutaraldehyde fixation for water-window XRM and concluded that this method is not able to prevent radiation damage in algal cells, and furthermore that an uptake of glutaraldehyde alters the distribution of x-ray absorption in the fixed cells. In an earlier example, Ref. [103] showed that radiation damage on *Vicia faba* chromosomes was clearly visible at doses of about $1-2 \cdot 10^5$ Gy, depending on the type of fixative.

Chemical fixation has been demonstrated in laboratory XRM in the water window. Examples include 3T3 fibroblasts fixed in glutaraldehyde [31] and COS-7 cells fixed on a Si₃N₄ membrane using ethanol in increasing concentration [104].

3. Wet Samples

Imaging of wet samples has been routinely done at synchrotron-based x-ray microscopes, on a wide range of samples, from cells to soils. Kirz and Jacobsen [105] summarize many early applications from NSLS at Brookhaven and BESSY in Berlin. Laboratory water-window XRM of wet samples has also been demonstrated on cells in cell medium [91] and aqueous soil samples [106]. Due to the vacuum conditions, the liquid has to be contained somehow, which is realized by putting the sample between two Si₃N₄ windows and gently clamping them together [107].

4. Cryo-Fixed Samples

For biological samples, cryo-fixation is the preferred preparation method. It is extensively used at synchrotron-based x-ray microscopes, e.g., [3,4,32–34,108]. Even though freezing biological material risks affecting the sample, a sufficiently fast transition into solid state creates vitreous (i.e., amorphous) ice, which keeps the structures intact [109–111]. This way the samples are imaged in their near-native state. The method is particularly attractive for water-window microscopy, with its natural contrast mechanism. Cryo-fixation has two main purposes: First, the sample is spatially fixed, which is necessary because the exposure times range from seconds to minutes. Second, at these low temperatures the sample is considerably more resistant to radiation damage. Cryo-fixed cells have been exposed to up to 10^{10} Gy in XRM without showing any observable morphological alterations [110]. In order to achieve high-resolution images with reasonable noise levels, it can be estimated that a dose on the order of 10^5 – 10^8 Gy is needed [109]. For hydrated biological samples at room temperature, numerical calculation and experimental results estimate that significant radiation damage occurs at $\sim 10^4$ Gy [112].

In order to form vitreous ice, the cooling rate needs to be higher than 10^4 K/s [113]. There is a range of different methods to achieve this, e.g., high-pressure freezing, jet freezing and slam freezing. However, the most commonly used method in XRM is plunge freezing in a liquid cryogen (usually ethane). The samples are typically placed on gold or copper TEM grids, coated with a thin holey carbon layer on one side. These grids can be picked up using tweezers and put into the plunge-freezing arrangement.

Ethane is a good choice of cryogen due to the large interval between its melting temperature (90 K) and boiling temperature (184 K). This decreases the risk of vaporization as small amounts of heat are transferred from the plunged sample. In fact, ethane has been shown to provide the fastest cooling rate in comparisons between different cryogens [114,115]. In contrast, plunging a room-temperature sample into liquid nitrogen (liquid from 63 to 77 K) will result in the formation of an insulating vapor layer, which considerably decreases the cooling rate.

One of the main challenges in cryo-fixation for soft XRM is to achieve an appropriate ice thickness. First of all, the ice layer should not exceed ~ 10 μm to avoid crystalline ice formation [112]. Second, the x-ray transmission through the ice will decrease with increasing thickness. As an example, a 10 μm layer of pure water ice gives about 30% transmission for $\lambda = 2.48$ nm, and a typical cell medium will transmit even less, depending on glucose concentration, etc. As pointed out above, this is especially important for laboratory x-ray microscopes, where the x-ray flux is limited. A too-thin ice layer, on the other hand, can give shadow effects and unwanted illumination gradients around the specimen or, in the worst case, structural changes due to dehydration.

In order to achieve the desired ice thickness, it is necessary to monitor the sample during the plunge-freezing procedure, preferably through an optical microscope [11,112]. The liquid layer on the sample is usually adjusted by blotting the sample grid using filter paper [116]. Several plunge-freezing systems are commercially available today, with built-in microscopes, adjustable humidity, automatic blotting and plunging, and an overall controlled procedure [117,118]. Both the Stockholm and Berlin laboratory x-ray microscopes rely on home-built simple plunge-freezing arrangements. Here, the sample is held by tweezers and plunge-frozen in liquid ethane with a speed of ~ 1 m/s. A camera with a lens system

is used to monitor the sample. Using oblique illumination on the grid, it is possible to observe when the liquid layer becomes thinner than the depth of the wells (10 μm), determining a suitable time for the plunge. We note that the optimal settings are different from sample to sample, and significant experimental optimization is often necessary.

F. Tomography

An ultimate goal of laboratory x-ray microscopes is to utilize the high x-ray penetration depth together with the high resolution and natural contrast to perform 3D imaging, through CT. The CT concept has been explored in great detail and is widely used in fields like clinical diagnostics and material science, but also for synchrotron-based XRM, e.g., [3,4,7,8]. However, when it comes to laboratory soft XRM, there are a few intrinsic issues that need to be resolved. In this section, we discuss the general concept of laboratory water-window x-ray tomography, the main challenges, and possible solutions.

1. General

The principles of constructing a 3D volume from a number of 2D projections acquired at different observation angles, is well known and can be found in standard textbooks [119]. The theory can be simplified by dividing the 3D object into thin 2D slices (giving 1D projections), which are treated independently. The results are easily transferred to the 3D case by stacking the reconstructed 2D slices.

It can be shown that each 1D projection, when Fourier-transformed, corresponds to a straight line in the Fourier transform of the 2D object, passing through the origin at an angle θ equal to the projection angle. This is known as the *Fourier slice theorem*. Complete information about the spatial-frequency content of the object can be obtained by gradually rotating and acquiring (an infinite number of) projections over a range of 0° – 180° . Building on this theory, the Crowther criterion [120] for the highest achievable resolution can be derived,

$$\Delta x = \frac{1}{\nu_c} \geq \frac{\pi D}{N}. \quad (5)$$

It estimates the smallest resolvable period Δx , or the highest spatial frequency ν_c , of the reconstructed object of diameter D , using N equally spaced projections from 0° to 180° . Naturally, the applicability of the Crowther criterion assumes that the individual projections are sampled sufficiently densely so as not to limit the resolution.

2. Laboratory Water-Window X-Ray Tomography

Even though the concept is clear, 3D imaging is not yet routine in laboratory soft x-ray microscopes. Here we identify and discuss three main issues: acquisition time, missing wedge, and DOF.

As mentioned before, the photon flux is a limiting factor in laboratory XRM. Tomographic reconstruction of thick objects with high resolution requires at least around 100 images (projections), which translates to significantly longer exposure time than for 2D imaging. As an example, consider imaging a 5 μm diameter object with 100 nm full-period resolution. According to Eq. (5), this requires 157 equally spaced angles from 0° to 180° . If we can limit each exposure to 5 s, the total exposure time becomes about 13 min.

In addition to the exposures, repositioning of the sample and refocusing might further increase the total data acquisition time. This can, however, be resolved by making sure that the position of the object coincides with the axis of rotation. Note that this alignment needs to be accurate within a couple of micrometers for the object to stay in focus at the higher angles. A systematic way to achieve this in a laboratory x-ray microscope has been developed by TU Berlin (cf. Section 4.A), by incorporating a visible-light microscope in the sample stage arrangement.

The second issue is the limited range of tilts, leading to a so-called *missing wedge*. In many imaging applications, the sample cannot be rotated more than about $\pm 60^\circ$ [4,11], resulting in a missing wedge of 60° . This will reduce the achievable resolution of the reconstruction along the optical axis of the microscope. There are different reasons as to why the higher tilt angles are not available. The rotation of the sample holder can be physically blocked by the objective. However, this can be partly resolved by using a microzone plate with large enough focal length, and/or a slimmer sample holder. Further, the illumination can be blocked by structures surrounding the region of interest. This happens, e.g., close to the grid lines on a metal TEM grid, or if the individual specimens on a sample grid are too close together. The most challenging reason, however, is the fact that a flat sample at an oblique angle gives a large projected thickness that simply absorbs too many photons. Many samples, like adherent cells, require a flat surface with an even layer of cell medium, and cryo-fixation prior to imaging. Hence, the projected ice layer thickness at high tilt angles will limit the tilt range. Attempts to resolve this issue include putting the sample inside or onto a glass capillary that can be rotated 180° [121,122]. However, this is not suitable for many types of samples, like adherent cells or in cell–cell interaction studies. In addition, the few-100-nm thick capillary walls will contribute appreciably to the absorption of the soft x-rays, which can increase the exposure times of the flux-limited laboratory-based microscopes. Another solution is double-tilt tomography [123]. It suggests merging two tilt series acquired around two orthogonal axes. This would in theory be possible to implement in laboratory XRM, but puts even higher demands on the photon flux, sample stage movement, and alignment. Finally, there are advanced reconstruction algorithms that include information on the missing wedge and/or assumptions about the sample properties, thereby restoring missing 3D information and reducing image artifacts [124,125].

As a final point, we discuss the issue of a limited DOF, which is inherent in all zone-plate-based imaging. A typical high-resolution zone plate ($\Delta r = 30$ nm for $\lambda = 2.48$ nm) has a DOF of < 1 μm , and even though fairly high resolution can be achieved at moderate distances from the DOF, this becomes a problem for thick samples like whole cells. One possibility is to use a larger outermost zone width, e.g., $\Delta r = 40$ nm, with the corresponding loss of resolution and NA. A suitable compromise must be considered for each imaging application. Focus-stack back-projection (FSBP) [126] has been suggested as a solution. It was shown that the contrast and resolution of a reconstructed object larger than the DOF can be improved by acquiring images at three defocus positions (-3 , 0 , $+3$ μm) relative to the center, for each tilt angle. For a fair comparison, the same total photon flux (i.e., exposure time) was used for the comparison. The method has been tested at a synchrotron, but not yet in a laboratory microscope.

G. System Considerations and Summary

Water-window XRM is a photon-hungry method. Typically, it is necessary to detect 100–1000 photons per pixel for good signal-to-noise 2D imaging. Thus, the high spectral brightness provided by synchrotron-radiation sources is a great advantage for this type of microscopy, since it relaxes the requirements of the optical system, alignment, filters, sample preparation, etc. A laboratory water-window microscope is bound to operate with a source of much lower brightness. Consequently, every microscope component must be optimized to allow high-resolution imaging with short exposure times. Here “high resolution” should aim at a few tens of nanometers, else the advantage compared to visible-light microscopes is too small. “Short exposure times” should preferably be below a few tens of seconds for 2D imaging and below a few tens of minutes for 3D tomography, to allow screening of large sample volumes and avoid thermal and other drifts that destroy resolution. Finally, we note that reliability and stability is of key importance in order to perform relevant biological imaging. Such imaging typically requires screening large volumes of samples before finding the interesting areas for imaging.

To date, two laboratory soft x-ray microscopes are approaching this goal, at KTH/Stockholm and at TU Berlin. Both are based on the same system design, including a high-power-laser liquid-jet laser-plasma, high-reflectivity normal-incidence multilayer condenser optics, high-resolution zone-plate optics, CCD detection, and a tailored cryogenic sample environment. The design allows high-resolution cryo-imaging in both 2D and 3D with short exposure times. The two key recent improvements enabling this compared to the early designs [10,91] are the higher-power laser plasma [79] and the high-reflectivity multilayer condenser mirror [88]. Although reliability is not yet at the level of a commercial instrument, the microscopes now can be trusted to provide hundreds of images when samples are available. In the next section, we describe the design of these two microscopes.

4. LABORATORY WATER-WINDOW X-RAY MICROSCOPY IN 2D AND 3D

A. Stockholm and Berlin Microscopes

Here we describe the Stockholm and Berlin laboratory full-field transmission soft x-ray microscopes. They are based on the same principle of operation, but with some individual features. The basic arrangement of these microscopes is shown in Fig. 5.

The x-ray source is a liquid nitrogen (LN_2) jet laser plasma, driven by a $\lambda = 1064$ nm diode-pumped Nd:YAG slab laser (Fraunhofer ILT, Aachen) [127], with ~ 0.5 ns and ~ 100 mJ pulses at a repetition rate of 2.0 kHz and 1.3 kHz for the two systems, respectively. The liquid jet is created by letting high-purity gaseous nitrogen pass under a few tens of bars of pressure through

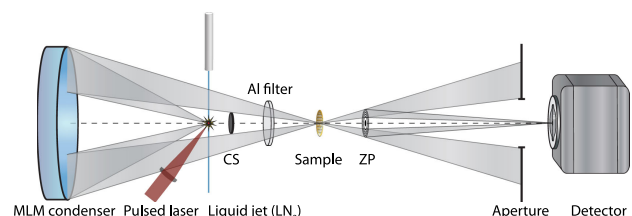


Fig. 5. Experimental arrangement of the laboratory water-window microscopes at KTH/Stockholm and TU Berlin. MLM, multilayer mirror; LN_2 , liquid nitrogen; CS, central stop; ZP, zone plate.

an LN₂-cooled cryostat before being ejected into the vacuum of the microscope through a 20–30 μm diameter glass capillary nozzle. The resulting plasma source emits primarily line emission from hydrogen- and helium-like nitrogen, including the strong line at $\lambda = 2.48$ nm from NVII K_{α} [79]. This $E = 500$ eV line has a reasonably narrow bandwidth ($E/\Delta E = 500\text{--}1000$), making it suitable for zone-plate imaging [128]. Furthermore, the line lies in the higher-energy part of the water window, with its appropriate transmission for many cell-biological applications.

Both microscopes use a 58-mm diameter, spherical multilayer condenser mirror, with a radius of curvature of 350 mm (OptiX fab, Jena). These state-of-the-art normal-incidence Cr/V mirrors have an average reflectivity of $>4\%$ at $\lambda = 2.48$ nm [11,88,89]. In addition to collecting the x-rays to illuminate the sample, the multilayer mirror selects the $\lambda = 2.48$ nm emission line from the broadband plasma with a bandwidth of $\lambda/\Delta\lambda = 450$. This creates the monochromaticity needed by the high-resolution zone-plate objective. A central stop and a 200 nm Al filter are placed in front of the sample, creating the hollow-cone illumination and removing visible stray light, respectively.

The microscopes use Ni or Au zone-plate objectives, with diameters and outermost zone widths depending on the specific application. As an example, a 200 μm diameter, 30 nm outermost zone width zone plate provides a long working distance (2.4 mm), which is suitable for tomography [11]. On the other hand, a diameter of 100 μm and outermost zone width of 25 nm can produce slightly better resolution and reduces the risk of chromatic aberrations [86].

The image is formed on a cooled, back-illuminated CCD detector, providing a high quantum efficiency for the $\lambda = 2.48$ nm x-rays, as well as low electronic noise. 2048 pixels \times 2048 pixels with a size of 13.5 μm make up the field of view, which is adjusted, depending on application, by moving the detector. Typical magnifications are $M = 600\text{--}1300$, giving a field of view of 21–46 μm.

The sample is held by a modified TEM goniometer cryo-stage (Bruker ASC in Berlin and FEI in Stockholm), which allows movement in all directions, as well as tilt along one axis. The Berlin microscope has also incorporated a visible-light microscope, in a vertical arrangement that images the sample inside vacuum. This visible-light microscope has two main purposes. It provides an overview of the sample, which makes it easier for the user to find regions of certain interest and thereby saves valuable experiment time. Further, it can be used together with fine positioning of the zone plate, using a piezo-driven three-axis stage to align the focus of the zone plate with the axis of rotation. This means that the sample will stay in position and in focus during rotation in tomographic imaging, thereby again saving valuable experiment time. The Stockholm microscope has a similar, but more primitive, visible-light microscope, primarily to monitor the relative position of the sample and zone plate. With its higher x-ray flux and shorter exposure times, searching the sample for regions of interest is instead done directly with x-rays. Still, a Berlin-style microscope is preferable and will be included in the Stockholm microscope to speed up tomographic data acquisition.

As discussed in Section 3.C, the diffraction-limited resolution of a zone-plate-based microscope depends on the outermost zone width. This, of course, requires that other factors, such as chromatic aberrations, astigmatism, vibrations, and photon noise, are not limiting. Both the Berlin and Stockholm microscopes show

close to diffraction-limited resolution, resolving features down to 20–25 nm in Au Siemens star test samples. Images acquired at both microscopes are shown in Fig. 6. The Berlin microscope used a 25-nm zone plate, a magnification of 1300 \times and 120-s exposure [Fig. 6(a)], while the Stockholm microscope used a 30-nm zone plate, a magnification of 1000 \times , and 60-s exposure [Fig. 6(b)]. The contrast transfer analysis in Fig. 6(c) shows the principal similarities between the microscopes but also indicates a nonnegligible difference for midspatial frequencies, which cannot be explained by the difference in parameters mentioned above. It is not fully understood. The different quality of the zone plates and Siemens stars used may certainly have an influence, but factors like the alignment and magnification could also contribute. The contrast transfer functions (CTFs) will now be further investigated by a quantitative cross-comparison of the two microscopes.

Short exposure times are of key importance for applying laboratory soft x-ray microscope to biology. Currently, cryo-fixed cell samples can be imaged with high quality using 10–30 s exposures in the Stockholm microscope and a few minutes in the Berlin microscope. This enables investigation of complex biological systems, where many samples need to be imaged. Equally important for the complex biological applications is a stable and reliable operation, allowing microscopy to be performed on an everyday basis. This has been improved greatly in the last few years. Examples of applications demonstrating the capabilities of the Berlin and Stockholm laboratory x-ray microscopes, are given below.

B. Dry Imaging

Imaging of dry samples is mainly done to verify the performance of the laboratory TXMs. Typical samples include test objects like Siemens stars (cf. Fig. 6), gratings, nanoparticles, or diatoms. Diatoms are popular test objects due to their radiation resistance, appropriate size, and intricate 3D structures. Consequently, they were extensively used early in laboratory XRM [10,129]. Figure 7(a) shows diatom imaging revealing features in the sub-100-nm range.

Figures 7(b) and 7(c) display a rare example of dry imaging with biological relevance. Here, the effects of high-pressure treatment on bacterial endospores of the *Bacillus subtilis* strain PS832 were investigated for applications in industrial food sterilization [130]. In Figs. 7(b) and 7(c), we compare the *B. subtilis* endospores before and after high-pressure treatment, respectively.

C. Wet Imaging

Laboratory water-window XRM has been applied to wet imaging, both on cells in aqueous environments [91] and on various types of colloids and soil samples [106]. Figures 8(a) and 8(b) show a comparison of Montmorillonite clay, imaged under dry and wet conditions, respectively. The images show that the structures in the wet sample, consisting of small stacked platelets, collapse as the clay dries. Figure 8(c) shows another example consisting of chernozem soil in aqueous solution. These images were acquired at rather high magnification (1300 \times) and an estimated resolution down to 30 nm (half-period) [106]. However, exposure times of a few minutes were required to achieve high image quality in this early version of the Stockholm laboratory x-ray microscope.

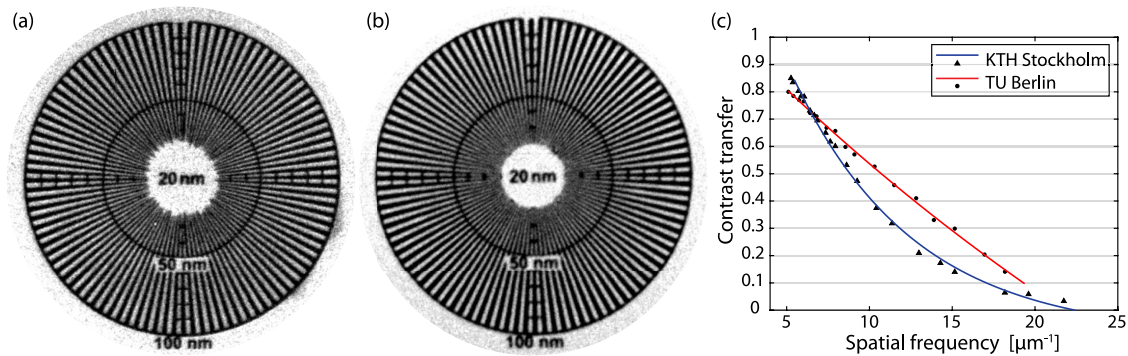


Fig. 6. Characterization of the optical performance by Au Siemens star imaging. (a) Siemens star imaged by the Berlin laboratory x-ray microscope, with 120 s exposure time; (b) Siemens star imaged by the Stockholm laboratory x-ray microscope with 60 s exposure time; (c) CTFs for the Berlin microscope and Stockholm microscope.

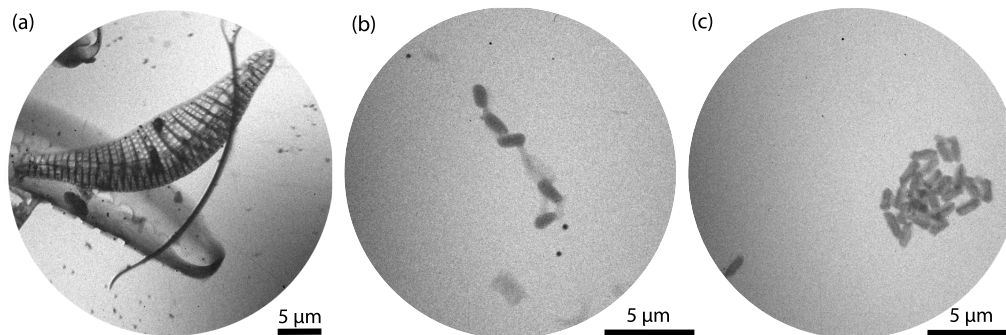


Fig. 7. Dry imaging with laboratory soft XRM. (a) Diatoms, exposure time 60 s. *B. subtilis* endospores (b) before and (c) after high-pressure treatment (exposure times 120 s and 180 s). Images from the Berlin microscope.

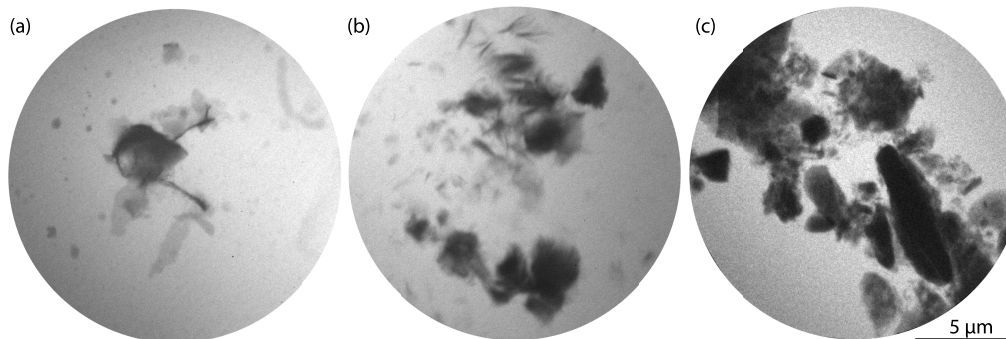


Fig. 8. Wet imaging with laboratory soft XRM. Montmorillonite clay samples imaged (a) dry and (b) in aqueous solution, for comparison; (c) chernozem soil in aqueous solution; exposures times range from 180 s to 360 s. Images from an early version of the Stockholm microscope.

D. 2D Cryo Imaging

Following the synchrotron-based soft x-ray microscopes [3,4], cryo-imaging at a laboratory microscope was first demonstrated on yeast and B-cells [131,132]. These early experiments suffered from long exposure times and significant experimental difficulties, making the iterative imaging typically necessary for biological studies impossible. The laboratory microscopes are now approaching maturity, allowing studies of relevant biological samples. Below we describe four recent and emerging biological investigations demonstrating this new level of laboratory soft x-ray microscope performance.

HEK 293 T cells in different stages of starvation have been imaged in 2D and 3D with 2D exposure times in the range of 10–30 s [11]. Figures 9(a) and 9(b) show two examples. The natural contrast allows observation of several structural changes as the starvation process progresses. Healthy cells typically adhere to the substrate with lamellipodia extended over the holey carbon surface. Starving cells show withdrawal of lamellipodia and the emergence of an increasing number of carbon-dense vesicles with diameters typically around 0.4–0.8 μm . Cells starved until the verge of cell death appear round and vacuolated. The carbon-dense structures may be related to autophagy, which can be induced by cell starvation [133,134].

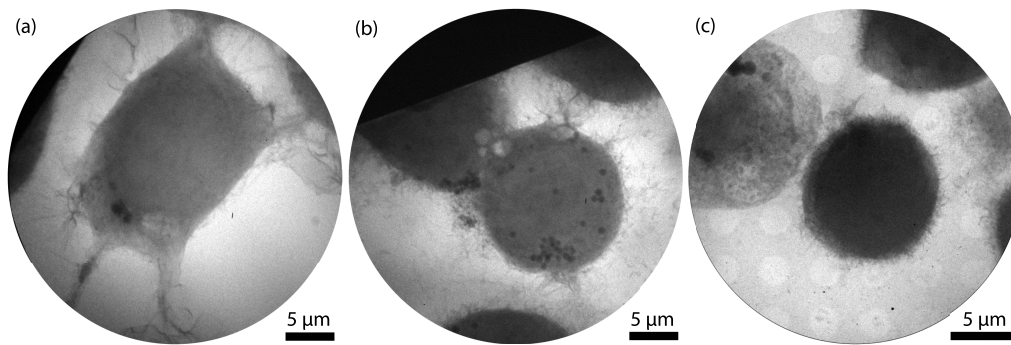


Fig. 9. 2D cryo imaging with laboratory soft XRM. (a) Healthy and adhered HEK 293 T cell, 30 s exposure time; (b) slightly starved and rounded HEK 293 T cell, 20 s exposure time; (c) THP-1 cells with 5 min exposure time. Images (a) and (b) from the Stockholm microscope and (c) from the Berlin microscope.

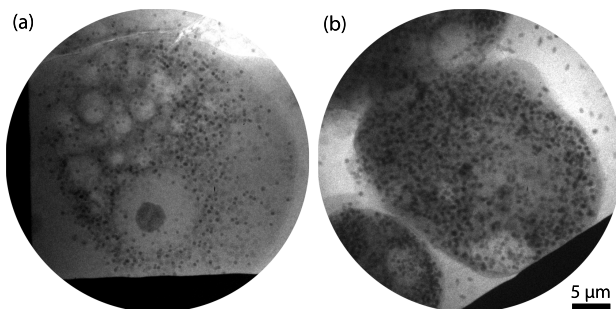


Fig. 10. 2D virus dynamics cryo imaging with laboratory soft XRM. (a) Healthy *Acanthamoeba castellanii*, 30 s exposure time; (b) *Acanthamoeba castellanii*, infected by giant DNA virus and imaged 24 h post-infection, 30 s exposure time. Images from the Stockholm microscope.

THP-1 cells have been suggested as a suitable model system for investigating the uptake, accumulation, and location of very small superparamagnetic iron oxide nanoparticles (VSOPs) via their interaction with the extracellular matrix (ECM). VSOPs have shown high affinity to glycosaminoglycans, which are key components of the ECM in atherosclerotic lesions. Figure 9(c) shows a first example of water-window THP-1 cell imaging, with the hairy structure representing the ECM of the THP-1 cell.

The discovery of giant DNA viruses has challenged the traditional view of viruses during the last 15 years [135,136]. These viruses are larger (up to 1.5 μm) and contains a more complex

genome than many cellular microbes. Cryogenic water-window XRM enables unique and near-native imaging of these giant viruses during their replication cycle inside a host. In such an investigation, the Stockholm laboratory x-ray microscope was used to study the dynamics of a newly discovered giant DNA virus, the Cedratvirus genus of *Pithoviridae* [137]. The infection process of this virus in the amoeba *Acanthamoeba castellanii* was imaged at 10 different times ranging from 6 to 72 h. As examples of this study, we show images of the amoeba showing no signs of infection [Fig. 10(a)] and a virus-infected amoeba about 24 h post infection, where the giant DNA virus particles can be seen throughout the cell as well as in the surrounding medium [Fig. 10(b)]. The high natural contrast allows for quantitative analysis of the infection dynamics.

The interaction between NK cells of the innate immune system and HEK 293 T cells has been studied in both 2D and 3D [11]. One example from this study is shown in Fig. 11(a). Different stages of the NK-mediated cell killing process were observed from the immune synapse formation stages to the onset of apoptosis and subsequent cell death. When performing cell–cell interaction studies, the long-term stability of the x-ray source is of great importance, as several TEM grids need to be searched in order to find cells in different stages of the immune synapse formation and cell death [138,139].

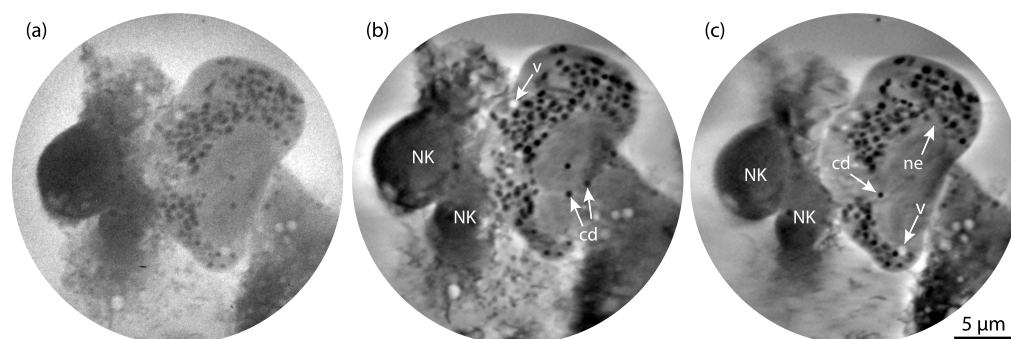


Fig. 11. Comparison between 2D and 3D imaging. (a) 2D imaging of two NK cells interacting with a starved HEK 293 T cell. This is one of the 10 s projections. (b) and (c) Two slices from the reconstructed 3D volume. Vacuoles (v), nuclear envelope (ne), and carbon-dense vesicles (c) and (d) are marked. Adapted from Ref. [11]. Images from the Stockholm microscope.

E. 3D Cryo-Tomography

The first tomography [129] as well as cryo tomography [130,131] at a laboratory soft x-ray microscope was performed at an early version of the Stockholm microscope. Although exposure times were long (hours) and the experimental effort significant for each 3D image, it proved the principle (see [Visualization 1](#) and [Visualization 2](#)).

Our present microscopes allow complex biological samples to be investigated. Recent work includes 3D cryo-imaging of starving HEK cells as well as NK–cell–HEK cell interaction [11]. Here, typically 70 projections were recorded with exposure times of 10–20 s per projection. Reconstruction was performed with a SIRT algorithm (simultaneous iterative reconstruction technique) (see [Visualization 3](#) and [Visualization 4](#)). Figure 11 shows the importance of 3D by comparing sections of the 3D volume [Figs. 11(b) and 11(c)] with a 2D projection [Fig. 11(a)]. It is clear from the comparison that 3D imaging provides a much more detailed image, in addition to the full volume information.

5. CONCLUSIONS AND OUTLOOK

Laboratory water-window XRM is reaching the maturity to allow biological studies of high relevance. In the present review, we have quantitatively and qualitatively compared and evaluated the key components of such microscopes as well as the system design. We find that the laboratory source brightness is the most critical parameter, but still all components as well as the full system design must be optimized to allow imaging with adequate exposure times and high resolution. Equally important for biological investigations is reliability and appropriate sample preparation.

Water-window XRM is unique among the microscopies in that it allows 10-nm-range 3D imaging of unstained intact cellular samples in their near-native state. During the past decade, synchrotron-based x-ray microscopes have demonstrated their importance for biological research. Of particular significance is their unique capacity for quantitative characterization of cellular and subcellular organization in single cells as well as in cell–cell interaction [140]. This spans external to internal morphology, such as lipid bodies, vacuoles, mitochondria, nuclear organization, etc. In addition, correlative light microscopy can provide molecular information that together with the primarily morphological x-ray data provides further insight in cell function. Unfortunately, there are only few available soft x-ray microscopes world-wide presently at synchrotron-radiation facilities [140]. Although the quality of the synchrotron microscopes is superior, having access to water-window microscopy in the home laboratory would increase the impact of the method, enable direct and parallel use of complementary methods, and extend the applicability via, e.g., optimized sample preparation techniques. In addition to being a stand-alone tool, laboratory x-ray microscopes should allow valuable screening of large sample volumes in order to make subsequent synchrotron-based experiments with limited beam time more effective.

As discussed above, state-of-the-art laboratory water-window XRM presently provides 10–20 s exposure time in 2D and 10–20 min in 3D. This is adequate for biological studies, but naturally, shorter would be better. We believe exposure times can be further reduced by a factor of 4–5. The laser-plasma source has potential for a 2× improvement by stabilization of the jet in combination with slightly higher laser power. The multilayer condenser mirror

has potential for 20%–30% higher average reflectivity, and we estimate the same goes for the zone plate. The resulting few-second and few-minute exposures in 2D and 3D, respectively, would not only be exciting, but it would also reduce system thermal stability requirements.

Although improving exposure time is attractive, we note that total data acquisition time is already longer than the exposure times. Sample preparation and change of sample is a manual and time-consuming activity that reduces throughput. Thus, improving this workflow has high priority. Equally important is improving the robustness and reliability of the system. Imaging large ensembles of biological material requires a high up-time. Here the key issues are laser and liquid jet stability.

Funding. Vetenskapsrådet; Knut och Alice Wallenbergs Stiftelse; Deutsche Forschungsgemeinschaft (SFB 1340).

Acknowledgment. The authors are indebted to many past and present coworkers for their contributions to the development of laboratory water-window microscopy to its present standard. In Stockholm: Lars Rymell, Magnus Berglund, Göran Johansson, Anders Holmberg, Heide Stollberg, Per Takman, Magnus Lindblom, Olof von Hofsten, Michael Bertilsson, Julia Reinspach, Fredrik Uhlén, Dale Martz, Jussi Rahomäki, Mårten Selin, Komang Arsana, and Thomas Frisk; in Berlin: Birgit Kanngiesser, Felix Weiss, Oliver Reichel, Johannes Tümmeler, Daniel Grötzsch, Jonas Baumann, Herbert Legall, Paul Kastl, Vladimir Usatkov, Antje Ludwig, Shailey Twamley, Gerd Schneider, Stefan Rehbein, Peter Guttmann; in Aachen: Marco Hoefler and Dominik Esser; and in Jena: Torsten Feigl.

Disclosures. The authors declare that there are no conflicts of interest related to this paper.

†These authors contributed equally to this work.

REFERENCES

1. A. Sakdinawat and D. Attwood, "Nanoscale x-ray imaging," *Nat. Photonics* **4**, 840–848 (2010).
2. C. Jacobsen, *X-Ray Microscopy* (Cambridge University, 2019).
3. M. Uchida, G. McDermott, M. Wetzler, M. A. Le Gros, M. Myllys, C. Knoechel, A. E. Barron, and C. A. Larabell, "Soft x-ray tomography of phenotypic switching and the cellular response to antifungal peptoids in *Candida albicans*," *Proc. Natl. Acad. Sci. USA* **106**, 19375–19380 (2009).
4. G. Schneider, P. Guttmann, S. Heim, S. Rehbein, F. Mueller, K. Nagashima, J. B. Heymann, W. G. Müller, and J. G. McNally, "Three-dimensional cellular ultrastructure resolved by x-ray microscopy," *Nat. Methods* **7**, 985–987 (2010).
5. H. N. Chapman and K. A. Nugent, "Coherent lensless x-ray imaging," *Nat. Photonics* **4**, 833–839 (2010).
6. S. Kapishnikov, A. Weiner, E. Shimoni, P. Guttmann, G. Schneider, N. Dahan-Pasternak, R. Dzikowski, L. Leiserowitz, and M. Elbaum, "Oriented nucleation of hemozoin at the digestive vacuole membrane in *Plasmodium falciparum*," *Proc. Natl. Acad. Sci. USA* **109**, 11188–11193 (2012).
7. A. Cruz-Adalia, G. Ramirez-Santiago, C. Calabia-Linares, M. Torres-Torresano, L. Feo, M. Galán-Díez, E. Fernández-Ruiz, E. Pereiro, P. Guttmann, M. Chiappi, G. Schneider, J. L. Carrascosa, F. J. Chichón, G. Martínez Del Hoyo, F. Sánchez-Madrid, and E. Veiga, "T cells kill bacteria captured by transinfection from dendritic cells and confer protection in mice," *Cell Host Microbe* **15**, 611–622 (2014).
8. M. A. Le Gros, E. J. Clowney, A. Magklara, A. Yen, E. Markenscoff-Papadimitrou, B. Colquitt, M. Myllys, M. Kellis, S. Lomvardas, and

- C. A. Larabell, "Soft x-ray tomography reveals gradual chromatin compaction and reorganization during neurogenesis in vivo," *Cell Rep.* **17**, 2125–2136 (2016).
9. M. Harkiolaki, M. C. Darrow, M. C. Spink, E. Kosior, K. Dent, and E. Duke, "Cryo-soft x-ray tomography: using soft x-rays to explore the ultrastructure of whole cells," *Emerg. Top. Life Sci.* **2**, 81–92 (2018).
10. M. Berglund, L. Rymell, M. Peuker, T. Wilhein, and H. M. Hertz, "Compact water-window transmission x-ray microscopy," *J. Microsc.* **197**, 268–273 (2000).
11. E. Fogelqvist, M. Kördel, V. Carannante, B. Önfelt, and H. M. Hertz, "Laboratory cryo x-ray microscopy for 3D cell imaging," *Sci. Rep.* **7**, 13433 (2017).
12. E. Spiller, R. Feder, J. Topalian, D. Eastman, W. Gudat, and D. Sayre, "X-ray microscopy of biological objects with carbon kappa and with synchrotron radiation," *Science* **191**, 1172–1174 (1976).
13. T. W. Ford, A. D. Stead, and R. A. Cotton, "Soft x-ray contact microscopy of biological materials," *Electron Microsc. Rev.* **4**, 269–292 (1991).
14. H. Kondo and T. Tomie, "Optimization of a laser-plasma x-ray source for contact x-ray microscopy," *J. Appl. Phys.* **75**, 3798–3805 (1994).
15. M. G. Ayele, P. W. Wachulak, J. Czwartos, D. Adjei, A. Bartnik, Wegrzynski, M. Szczurek, L. Pina, and H. Fiedorowicz, "Development and characterization of a laser-plasma soft x-ray source for contact microscopy," *Nucl. Instrum. Methods Phys. Res., Sect. B* **411**, 35–43 (2017).
16. M. Kishimoto, M. Kado, M. Ishino, S. Tamotsu, K. Yasuda, and K. Shinohara, "Development of single shot soft x-ray contact microscopy system for nano-scale dynamics measurement of living biological specimen," *AIP Conf. Proc.* **1465**, 43–47 (2012).
17. T. Ejima, M. Kado, M. Aoyama, K. Yasuda, and S. Tamotsu, "Organelle distribution in a hydrated bio-cell by correlation between soft x-ray and fluorescence images," *J. Phys. Conf. Ser.* **849**, 012009 (2017).
18. H. Azuma, A. Takeichi, and S. Noda, "Laser plasma soft x-ray contact microscopy of polymer composites," *Jpn. J. Appl. Phys.* **33**, 4622–4627 (1994).
19. P. C. Cheng, R. Feder, D. M. Shinozaki, K. H. Tan, R. W. Eason, A. Michette, and R. J. Rosser, "Soft x-ray contact microscopy," *Nucl. Instrum. Methods Phys. Res., Sect. A* **246**, 668–674 (1986).
20. Y. Wang and C. Jacobsen, "A numerical study of resolution and contrast in soft x-ray contact microscopy," *J. Microsc.* **191**, 159–169 (1998).
21. H. Rarback, J. M. Kenney, J. Kirz, M. R. Howells, P. Chang, R. Coane, R. Feder, P. J. Houzago, D. P. Kern, and D. Sayre, "Recent results from the Stony Brook scanning microscope," in *X-Ray Microscopy*, G. Schmahl and D. Rudolph, eds. Vol. 43 of Springer Series in Optical Sciences (Springer, 1984), pp. 203–215.
22. A. Gianoncelli, G. Kouroussias, L. Merolle, M. Altissimo, and A. Bianco, "Current status of the TwinMic beamline at Elettra: a soft x-ray transmission and emission microscope station," *J. Synchrotron Radiat.* **23**, 1526–1537 (2016).
23. M. A. Le Gros, G. McDermott, B. P. Cinquin, E. A. Smith, M. Do, W. L. Chao, P. P. Naulleau, and C. A. Larabell, "Biological soft x-ray tomography on beamline 2.1 at the advanced light source," *J. Synchrotron Radiat.* **21**, 1370–1377 (2014).
24. A. Leontowich, R. Berg, C. Regier, D. Taylor, J. Wang, D. Beauregard, J. Geilhufe, J. Swirsky, J. Wu, C. Karunakaran, A. Hitchcock, and S. Urquhart, "Cryo scanning transmission x-ray microscope optimized for spectrotomography," *Rev. Sci. Instrum.* **89**, 93704 (2018).
25. M. Salomé, M. Cotte, R. Baker, R. Barrett, N. Benseny-Cases, G. Berruyer, D. Bugnazet, H. Castillo-Michel, C. Cornu, B. Fayard, E. Gagliardini, R. Hino, J. Morse, E. Papillon, E. Pouyet, C. Rivard, V. A. Solé, J. Susini, and G. Veronesi, "The ID21 scanning x-ray microscope at ESRF," *J. Phys. Conf. Ser.* **425**, 182004 (2013).
26. B. Lai, D. Capatina, C. Roehrig, O. Antipova, Z. Cai, S. Chen, and J. Deng, "APS 2-ID microprobes: status and future plans," *Microsc. Microanal.* **24**, 332–335 (2018).
27. L. Lühl, K. Andrianov, H. Dierks, A. Haidl, A. Dehlinger, M. Heine, J. Heeren, T. Nisius, T. Wilhein, and B. Kanngießer, "Scanning transmission x-ray microscopy with efficient x-ray fluorescence detection (STXM-XRF) for biomedical applications in the soft and tender energy range," *J. Synchrotron Radiat.* **26**, 430–438 (2019).
28. A. G. Michette, R. E. Burge, A. M. Rogoyski, F. O'Neill, and I. C. E. Turcu, "The potential of laser plasma sources in scanning x-ray microscopy," in *X-Ray Microscopy II*, D. Sayre, J. Kirz, M. Howells, and H. Rarback, eds. (Springer, 1988), pp. 59–62.
29. J. A. Trail, R. L. Byer, and J. B. Kortright, "The Stanford tabletop scanning x-ray microscope," in *X-Ray Microscopy II*, D. Sayre, J. Kirz, M. Howells, and H. Rarback, eds. (Springer, 1988), pp. 310–315.
30. A. G. Michette, I. C. E. Turcu, M. S. Schulz, M. T. Browne, G. R. Morrison, P. Fluck, C. J. Buckley, and G. F. Foster, "Scanning x-ray microscopy using a laser-plasma source," *Rev. Sci. Instrum.* **64**, 1478–1482 (1993).
31. B. Niemann, D. Rudolph, and G. Schmahl, "X-ray microscopy with synchrotron radiation," *Appl. Opt.* **15**, 1883–1884 (1976).
32. A. Gal, A. Sorrentino, K. Kahil, E. Pereiro, D. Faivre, and A. Scheffel, "Native-state imaging of calcifying and noncalcifying microalgae reveals similarities in their calcium storage organelles," *Proc. Natl. Acad. Sci. USA* **115**, 11000–11005 (2018).
33. J. L. Carrascosa, F. J. Chichón, E. Pereiro, M. J. Rodríguez, J. J. Fernández, M. Esteban, S. Heim, P. Guttman, and G. Schneider, "Cryo-x-ray tomography of vaccinia virus membranes and inner compartments," *J. Struct. Biol.* **168**, 234–239 (2009).
34. E. Hanssen, C. Knoechel, N. Klonis, N. Abu-Bakar, S. Deed, M. Legros, C. Larabell, and L. Tilley, "Cryo transmission x-ray imaging of the malaria parasite, *P. falciparum*," *J. Struct. Biol.* **173**, 161–168 (2011).
35. W. Meyer-Ilse, G. Denbeaux, L. E. Johnson, W. Bates, A. Lucero, and E. H. Anderson, "The high resolution x-ray microscope, XM-1," *AIP Conf. Proc.* **507**, 129 (2000).
36. P. Guttman, S. Werner, S. Rehbein, C. Habel, and G. Schneider, "First results from the x-ray microscopy beamline U41-PGM1-XM at BESSY II," *Microsc. Microanal.* **24**, 204–205 (2018).
37. E. Pereiro, J. Nicolás, S. Ferrer, and M. R. Howells, "A soft x-ray beamline for transmission x-ray microscopy at ALBA," *J. Synchrotron Radiat.* **16**, 505–512 (2009).
38. G. Schmahl, B. Niemann, D. Rudolph, M. Diehl, J. Thieme, W. Neff, R. Holz, R. Lebert, F. Richter, and G. Herziger, "A laboratory x-ray microscope with a plasma x-ray source," in *X-Ray Microscopy III*, A. G. Michette, G. R. Morrison, and C. J. Buckley, eds. (Springer, 1992), pp. 66–69.
39. W. Neff, J. Eberle, R. Holz, F. Richter, and R. Lebert, "A plasma focus as radiation source for a laboratory x-ray microscope," in *X-Ray Microscopy II*, D. Sayre, J. Kirz, M. Howells, and H. Rarback, eds., Vol. 56 of Springer Series in Optical Sciences (Springer, 1988), pp. 22–29.
40. M. Benk, K. Bergmann, D. Schäfer, and T. Wilhein, "Compact soft x-ray microscope using a gas-discharge light source," *Opt. Lett.* **33**, 2359–2361 (2008).
41. D. B. Carlson, J. Gelb, V. Palshin, and J. E. Evans, "Laboratory-based cryogenic soft x-ray tomography with correlative cryo-light and electron microscopy," *Microsc. Microanal.* **19**, 22–29 (2013).
42. H. Legall, G. Blobel, H. Stiel, W. Sandner, C. Seim, P. Takman, D. H. Martz, M. Selin, U. Vogt, H. M. Hertz, D. Esser, H. Sipma, J. Luttmann, M. Höfer, H. D. Hoffmann, S. Yulin, T. Feigl, S. Rehbein, P. Guttman, G. Schneider, U. Wiesemann, M. Wirtz, and W. Diете, "Compact x-ray microscope for the water window based on a high brightness laser plasma source," *Opt. Express* **20**, 18362–18369 (2012).
43. P. W. Wachulak, A. Torrisi, W. Krauze, A. Bartnik, J. Kostecki, M. Maisano, A. M. Sciortino, and H. Fiedorowicz, "A 'water window' tomography based on a laser-plasma double-stream gas-puff target soft x-ray source," *Appl. Phys. B* **125**, 70 (2019).
44. M. Müller, T. Mey, J. Niemeier, and K. Mann, "Table-top soft x-ray microscope using laser-induced plasma from a pulsed gas jet," *Opt. Express* **22**, 23489–23495 (2014).
45. T. Ogata, K. Iimura, S. Aoki, Y. Yoshidomi, O. Mitomi, and K. Shinada, "Development of a grazing incidence soft x-ray microscope with a laser-produced plasma source," *J. Elec. Spectr. Rel. Phenom.* **80**, 357–360 (1996).
46. T. McEnroe, F. O'Reilly, P. Sheridan, J. Howard, R. Byrne, A. O'Connor, D. Rogers, C. Rogers, C. McCarthy, A. Manzoni, D. Skoko, and K. Fahy, "Development of a commercial laboratory scale soft x-ray microscope," *Microsc. Microanal.* **23**, 982–983 (2017).
47. K. W. Kim, Y. Kwon, K. Y. Nam, J. H. Lim, K. G. Kim, K. S. Chon, B. H. Kim, D. E. Kim, J. G. Kim, B. N. Ahn, H. J. Shin, S. Rah, K. H. Kim, J. S. Chae, D. G. Gweon, D. W. Kang, S. H. Kang, J. Y. Min, K. S. Choi, S. E. Yoon, E. A. Kim, Y. Namba, and K. H. Yoon, "Compact soft x-ray transmission microscopy with sub-50 nm spatial resolution," *Phys. Med. Biol.* **51**, N99–N107 (2006).

48. S. Ohsuka, A. Ohba, S. Onoda, K. Nakamoto, T. Nakano, M. Miyoshi, K. Soda, and T. Hamakubo, "Laboratory-size three-dimensional x-ray microscope with Wolter type I mirror optics and an electron-impact water window x-ray source," *Rev. Sci. Instrum.* **85**, 093701 (2014).
49. "Wayforlight," <https://www.wayforlight.eu/en/synchrotrons>.
50. "Advanced Light Source," <https://als.lbl.gov/machine-information/>.
51. K. Bergmann, F. Küpper, and M. Benk, "Soft x-ray emission from a pulsed gas discharge in a pseudosparklike electrode geometry," *J. Appl. Phys.* **103**, 123304 (2008).
52. S. F. Horne, J. Silterra, and W. Holber, "A compact soft x-ray microscope using an electrode-less Z-pinch source," *J. Phys. Conf. Ser.* **186**, 12028 (2009).
53. W. H. Bennett, "Magnetically self-focussing streams," *Phys. Rev.* **45**, 890–897 (1934).
54. R. Lebert, W. Neff, and D. Rothweiler, "Pinch plasma source for x-ray microscopy with nanosecond exposure time," *J. X-ray. Sci. Technol.* **6**, 107–140 (1996).
55. J. P. Boeuf and L. C. Pitchford, "Pseudospark discharges via computer simulation," *IEEE Trans. Plasma Sci.* **19**, 286–296 (1991).
56. V. Bakshi, "EUV source technology: challenges and status, Ch. 1," in *EUV Sources for Lithography*, V. Bakshi, ed. (SPIE, 2006), pp. 3–25.
57. N. Fu, Y. Liu, X. Ma, and Z. Chen, "EUV lithography: state-of-the-art review," *J. Microelectron. Manuf.* **2**, 19020202 (2019).
58. D. Attwood and A. Sakdinawat, "Physics of hot dense plasmas," in *X-Rays and Extreme Ultraviolet Radiation: Principles and Applications*, 2nd ed. (Cambridge University, 2016), Chap. 8, pp. 315–402.
59. R. Kodama, K. Okada, N. Ikeda, M. Mineo, K. A. Tanaka, T. Mochizuki, and C. Yamanaka, "Soft x-ray emission from ω_0 , $2\omega_0$, and $4\omega_0$ laser-produced plasmas," *J. Appl. Phys.* **59**, 3050–3052 (1986).
60. M. Hoshino and S. Aoki, "Laser plasma soft x-ray microscope with Wolter mirrors for observation of biological specimens in air," *Jpn. J. Appl. Phys.* **45**, 989–994 (2006).
61. J. Sheil, P. Dunne, T. Higashiguchi, D. Kos, E. Long, T. Miyazaki, F. O'Reilly, G. O'Sullivan, P. Sheridan, C. Suzuki, E. Sokell, E. White, and D. Kilbane, "Analysis of soft x-ray emission spectra of laser-produced dysprosium, erbium and thulium plasmas," *J. Phys. B* **50**, 065006 (2017).
62. L. Rymell and H. M. Hertz, "Laser-plasma droplet target for low-debris soft x-ray generation," *Opt. Commun.* **103**, 105–110 (1993).
63. L. Rymell, M. Berglund, and H. M. Hertz, "Debris-free single-line laser-plasma x-ray source for microscopy," *Appl. Phys. Lett.* **66**, 2625–2627 (1995).
64. M. Berglund, L. Rymell, H. M. Hertz, and T. Wilhein, "Cryogenic liquid-jet target for debris-free laser-plasma soft x-ray generation," *Rev. Sci. Instrum.* **69**, 2361–2364 (1998).
65. M. Wieland, T. Wilhein, M. Faubel, C. Ellert, M. Schmidt, and O. Sublemontier, "EUV and fast ion emission from cryogenic liquid jet target laser-generated plasma," *Appl. Phys. B* **72**, 591–597 (2001).
66. H. Fiedorowicz, A. Bartnik, Z. Patron, and P. Parys, "X-ray emission from laser-irradiated gas puff targets," *Appl. Phys. Lett.* **62**, 2778–2780 (1993).
67. E. Fogelqvist, M. Kördel, M. Selin, and H. M. Hertz, "Stability of liquid-nitrogen-jet laser-plasma targets," *J. Appl. Phys.* **118**, 174902 (2015).
68. J. F. Adam, J. P. Moy, and J. Susini, "Table-top water window transmission x-ray microscopy: review of the key issues, and conceptual design of an instrument for biology," *Rev. Sci. Instrum.* **76**, 091301 (2005).
69. B. Buijsse, "keV-electron-based table-top soft x-ray source," *Proc. SPIE* **4502**, 74–81 (2001).
70. P. Skoglund, U. Lundström, U. Vogt, and H. M. Hertz, "High-brightness water-window electron-impact liquid-jet microfocussing source," *Appl. Phys. Lett.* **96**, 084103 (2010).
71. V. Cardin, B. E. Schmidt, N. Thiré, S. Beaulieu, V. Wanie, M. Negro, C. Vozzi, V. Tosa, and F. Légaré, "Self-channelled high harmonic generation of water window soft x-rays," *J. Phys. B* **51**, 174004 (2018).
72. G. K. Tadesse, R. Klas, S. Dürmcher, S. Hädrich, I. Wahyutama, M. Steinert, C. Spielmann, M. Züchler, T. Pertsch, A. Tünnermann, J. Limpert, and J. Rothhardt, "High speed and high resolution table-top nanoscale imaging," *Opt. Lett.* **41**, 5170–5173 (2016).
73. A. Rockwood, Y. Wang, S. Wang, M. Berrill, V. N. Shlyaptsev, and J. J. Rocca, "Compact gain-saturated x-ray lasers down to 685 nm and amplification down to 585 nm," *Optica* **5**, 257–262 (2018).
74. M. Züch, R. Jung, C. Späth, J. Tümmler, A. Guggenmos, D. Attwood, U. Kleineberg, H. Stiel, and C. Spielmann, "Transverse coherence limited coherent diffraction imaging using a molybdenum soft x-ray laser pumped at moderate pump energies," *Sci. Rep.* **7**, 1–10 (2017).
75. F. Albert and A. G. R. Thomas, "Applications of laser wakefield accelerator-based light sources," *Plasma Phys. Controlled Fusion* **58**, 103001 (2016).
76. T. Helk, M. Züch, and C. Spielmann, "Perspective: towards single shot time-resolved microscopy using short wavelength table-top light sources," *Struct. Dyn.* **6**, 010902 (2019).
77. F. Brizuela, Y. Wang, C. A. Brewer, F. Pedaci, W. Chao, E. H. Anderson, Y. Liu, K. A. Goldberg, P. Naulleau, P. Wachulak, M. C. Marconi, D. T. Attwood, J. J. Rocca, and C. S. Menoni, "Microscopy of extreme ultraviolet lithography masks with 132 nm tabletop laser illumination," *Opt. Lett.* **34**, 271–273 (2009).
78. J. Wenz, S. Schleede, K. Khrennikov, M. Bech, P. Thibault, M. Heigoldt, F. Pfeiffer, and S. Karsch, "Quantitative x-ray phase-contrast microtomography from a compact laser-driven betatron source," *Nat. Commun.* **6**, 7568 (2015).
79. D. H. Martz, M. Selin, O. von Hofsten, E. Fogelqvist, A. Holmberg, U. Vogt, H. Legall, G. Blobel, C. Seim, H. Stiel, and H. M. Hertz, "High average brightness water window source for short-exposure cryomicroscopy," *Opt. Lett.* **37**, 4425–4427 (2012).
80. P. W. Wachulak, A. Bartnik, H. Fiedorowicz, P. Rudawski, R. Jarocki, J. Kostecki, and M. Szczurek, "'Water window' compact, table-top laser plasma soft x-ray sources based on a gas puff target," *Nucl. Instrum. Methods Phys. Res., Sect. B* **268**, 1692–1700 (2010).
81. P. W. Wachulak, A. Torrisi, A. Bartnik, D. Adjei, J. Kostecki, L. Wegrzynski, R. Jarocki, M. Szczurek, and H. Fiedorowicz, "Desktop water window microscope using a double-stream gas puff target source," *Appl. Phys. B* **118**, 573–578 (2015).
82. A. G. Michette, Z. Wang, N. I. Khaleque, and G. S. Dermody, "The King's College laboratory scanning x-ray microscope," *AIP Conf. Proc.* **507**, 420 (2000).
83. P. Wachulak, A. Torrisi, M. F. Nawaz, A. Bartnik, D. Adjei, Š. Vondrová, J. Turňová, A. Jančárek, J. Limpouch, M. Vrbová, and H. Fiedorowicz, "A compact 'water window' microscope with 60 nm spatial resolution for applications in biology and nanotechnology," *Microsc. Microanal.* **21**, 1214–1223 (2015).
84. L. Malmqvist, L. Rymell, M. Berglund, and H. M. Hertz, "Liquid-jet target for laser-plasma soft x-ray generation," *Rev. Sci. Instrum.* **67**, 4150–4153 (1996).
85. M. Born and E. Wolf, "Interference and diffraction with partially coherent light," in *Principles of Optics*, 7th ed. (Cambridge University, 1999), Chap. 10, pp. 554–632.
86. D. Attwood and A. Sakdinawat, "X-ray and extreme ultraviolet optics," in *X-Rays and Extreme Ultraviolet Radiation: Principles and Applications*, 2nd ed. (Cambridge University, 2016), Chap. 10, pp. 446–513.
87. H. Stollberg, S. Yulin, P. A. C. Takman, and H. M. Hertz, "High-reflectivity CrSc multilayer condenser for compact soft x-ray microscopy," *Rev. Sci. Instrum.* **77**, 123101 (2006).
88. T. Feigl, optiX fab, Hans-Knoell-Str. 6, 07745 Jena, Germany, www.optixfab.com (personal communication, 2020).
89. A. Dehlinger, J. Braenzel, D. Groetzsch, T. Feigl, R. Jung, B. KangieBer, S. Rehbein, C. Seim, and H. Stiel, "Towards high performance soft x-ray cryo-tomography in the laboratory," *Microsc. Microanal.* **24**, 250–251 (2018).
90. M. Benk, "Pinchplasma für die Mikroskopie mit weicher Röntgenstrahlung," Ph.D. thesis (Der Fakultät für Maschinenwesen, Rheinisch-Westfälische Technische Hochschule Aachen, 2011).
91. P. A. C. Takman, H. Stollberg, G. A. Johansson, A. Holmberg, M. Lindblom, and H. M. Hertz, "High-resolution compact x-ray microscopy," *J. Microsc.* **226**, 175–181 (2007).
92. O. von Hofsten, P. A. C. Takman, and U. Vogt, "Simulation of partially coherent image formation in a compact soft x-ray microscope," *Ultramicroscopy* **107**, 604–609 (2007).
93. A. V. Baez, "Resolving power in diffraction microscopy with special reference to x-rays," *Nature* **169**, 963–964 (1952).
94. G. Schmahl and D. Rudolph, "High power zone plates as image forming systems for soft x-rays," *Optik* **29**, 577–585 (1969).
95. B. Rösner, F. Koch, F. Döring, J. Bosgra, V. A. Guzenko, E. Kirk, M. Meyer, J. L. Ornelas, R. H. Fink, S. Stanescu, S. Swaraj, R. Belkhou, B. Watts, J. Raabe, and C. David, "Exploiting atomic layer deposition for

- fabricating sub-10 nm x-ray lenses," *Microelectron. Eng.* **191**, 91–96 (2018).
96. A. Lübcke, J. Braenzel, A. Dehlinger, M. Schnürer, H. Stiel, P. Guttman, S. Rehbein, G. Schneider, S. Werner, R. Kemmler, S. Ritter, M. Raugust, T. Wende, M. Behrendt, and M. Regehly, "Soft X-ray nanoscale imaging using a sub-pixel resolution charge coupled device (CCD) camera," *Rev. Sci. Instrum.* **90**, 043111 (2019).
97. W. S. Boyle and G. E. Smith, "Charge coupled semiconductor devices," *Bell Syst. Tech. J.* **49**, 587–593 (1970).
98. G. F. Amelio, M. F. Tompsett, and G. E. Smith, "Experimental verification of the charge coupled device concept," *Bell Syst. Tech. J.* **49**, 593–600 (1970).
99. W. Meyer-Ilse, T. Wilhein, and P. Guttman, "Thinned back-illuminated CCD for x-ray microscopy," *Proc. SPIE* **1900**, 241–245 (1993).
100. <https://andor.oxinst.com/products/high-energy-detection/ikon-l-so>.
101. S. Jearanaikoon and J. V. Abraham-Peskir, "An x-ray microscopy perspective on the effect of glutaraldehyde fixation on cells," *J. Microsc.* **218**, 185–192 (2005).
102. L. A. Finney and Q. Jin, "Preparing adherent cells for x-ray fluorescence imaging by chemical fixation," *J. Vis. Exp.* **2015**, 1–6 (2015).
103. S. Williams, X. Zhang, C. Jacobsen, J. Kirz, S. Lindaas, J. Van't Hof, and S. S. Lamm, "Measurements of wet metaphase chromosomes in the scanning transmission x-ray microscope," *J. Microsc.* **170**, 155–165 (1993).
104. H. M. Hertz, M. Berglund, G. A. Johansson, M. Peuker, T. Wilhein, and H. Brismar, "Compact water-window x-ray microscopy with a droplet laser-plasma source," *AIP Conf. Proc.* **507**, 721–725 (2000).
105. J. Kirz, C. Jacobsen, and M. Howells, "Soft x-ray microscopes and their biological applications list of figures," *Q. Rev. Biophys.* **28**, 33–130 (1995).
106. H. M. Hertz, M. Bertilson, O. von Hofsten, S. C. Gleber, J. Sedlmair, and J. Thieme, "Laboratory x-ray microscopy for high-resolution imaging of environmental colloid structure," *Chem. Geol.* **329**, 26–31 (2012).
107. H. Stollberg, M. Pokorny, and H. M. Hertz, "A vacuum-compatible wet-specimen chamber for compact x-ray," *J. Microsc.* **226**, 71–73 (2007).
108. G. Schneider and B. Niemann, "Cryo x-ray microscopy experiments with the x-ray microscope at BESSY," in *X-Ray Microscopy and Spectromicroscopy*, J. Thieme, G. Schmahl, E. Umbach, and D. Rudolph, eds. (Springer, 1998), pp. 25–34.
109. G. Schneider, B. Niemann, P. Guttman, D. Rudolph, and G. Schmahl, "Cryo x-ray microscopy," *Synchrotron Radiat. News* **8**, 19–28 (1995).
110. J. Maser, A. Osanna, Y. Wang, C. Jacobsen, J. Kirz, S. Spector, B. Winn, and D. Tennant, "Soft x-ray microscopy with a cryo scanning transmission x-ray microscope: I. Instrumentation, imaging and spectroscopy," *J. Microsc.* **197**, 68–79 (2000).
111. T. Beetz and C. Jacobsen, "Soft x-ray radiation-damage studies in PMMA using a cryo-STXM," *J. Synchrotron Radiat.* **10**, 280–283 (2003).
112. G. Schneider, "Cryo x-ray microscopy with high spatial resolution in amplitude and phase contrast," *Ultramicroscopy* **75**, 85–104 (1998).
113. P. Echlin, *Low-Temperature Microscopy and Analysis* (Springer, 1992).
114. K. P. Ryan, D. H. Purse, S. G. Robinson, and J. W. Wood, "The relative efficiency of cryogens used for plunge-cooling biological specimens," *J. Microsc.* **145**, 89–96 (1987).
115. K. P. Ryan, W. B. Bald, K. Neumann, P. Simonsberger, D. H. Purse, and D. N. Nicholson, "Cooling rate and ice-crystal measurement in biological specimens plunged into liquid ethane, propane, and Freon 22," *J. Microsc.* **158**, 365–378 (1990).
116. M. J. Dobro, L. A. Melanson, G. J. Jensen, and A. W. McDowall, "Plunge freezing for electron cryomicroscopy," *Methods Enzymol.* **481**, 63–82 (2010).
117. Leica Microsystems, "Automatic plunge freezer EM GP2," <https://www.leica-microsystems.com/products/sample-preparation-for-electron-microscopy/p/leica-em-gp2/>.
118. ThermoFisher Scientific, "Cryo EM sample preparation with the Vitrobot system," <https://www.fei.com/products/vitrobot-for-life-sciences/>.
119. J. Hsieh, *Computed Tomography: Principles, Design, Artifacts, and Recent Advances*, 2nd ed. (SPIE, 2009).
120. R. A. Crowther, D. J. DeRosier, and F. R. S. Klug, "The reconstruction of a three-dimensional structure from projections and its application to electron microscopy. II. Direct methods," *Proc. R. Soc. London B* **182**, 89–102 (1972).
121. D. Weiß, G. Schneider, B. Niemann, P. Guttman, D. Rudolph, and G. Schmahl, "Computed tomography of cryogenic biological specimens based on x-ray microscopic images," *Ultramicroscopy* **84**, 185–197 (2000).
122. M. A. Le Gros, G. McDermott, and C. A. Larabell, "X-ray tomography of whole cells," *Curr. Opin. Struct. Biol.* **15**, 593–600 (2005).
123. P. Penczek, M. Marko, K. Buttle, and J. Frank, "Double-tilt electron tomography," *Ultramicroscopy* **60**, 393–410 (1995).
124. Y. Deng, Y. Chen, Y. Zhang, S. Wang, F. Zhang, and F. Sun, "ICON: 3D reconstruction with 'missing-information' restoration in biological electron tomography," *J. Struct. Biol.* **195**, 100–112 (2016).
125. K. J. Batenburg and J. Sijbers, "DART: a practical reconstruction algorithm for discrete tomography," *IEEE Trans. Image Process.* **20**, 2542–2553 (2011).
126. M. Selin, E. Fogelqvist, S. Werner, and H. M. Hertz, "Tomographic reconstruction in soft x-ray microscopy using focus-stack back-projection," *Opt. Lett.* **40**, 2201–2204 (2015).
127. P. Russbuedt, D. Hoffmann, M. Höfer, J. Löhring, J. Luttmann, A. Meissner, J. Weitenberg, M. Traub, T. Sartorius, D. Esser, R. Wester, P. Loosen, and R. Poprawe, "Innoslab amplifiers," *IEEE J. Sel. Top. Quantum Electron.* **21**, 447–463 (2015).
128. T. Wilhein, D. Hambach, B. Niemann, M. Berglund, L. Rymell, and H. M. Hertz, "Off-axis reflection zone plate for quantitative soft x-ray source characterization," *Appl. Phys. Lett.* **71**, 190–192 (1997).
129. M. Bertilson, O. von Hofsten, U. Vogt, A. Holmberg, and H. M. Hertz, "High-resolution computed tomography with a compact soft x-ray microscope," *Opt. Express* **17**, 11057–11065 (2009).
130. C. Seim, K. Reineke, S. Werner, A. Dehlinger, H. Legall, H. Stiel, and B. Kannigießer, "High pressure treated *Bacillus subtilis* spores—structural analysis by means of synchrotron and laboratory based soft x-ray microscopy," *Innov. Food Sci. Emerg. Technol.* **29**, 134–142 (2015).
131. M. Bertilson, O. von Hofsten, U. Vogt, A. Holmberg, A. E. Christakou, and H. M. Hertz, "Laboratory soft-x-ray microscope for cryotomography of biological specimens," *Opt. Lett.* **36**, 2728–2730 (2011).
132. H. M. Hertz, O. von Hofsten, M. Bertilson, U. Vogt, A. Holmberg, J. Reinspach, D. Martz, M. Selin, A. E. Christakou, J. Jerlström-Hultqvist, and S. Svärd, "Laboratory cryo soft x-ray microscopy," *J. Struct. Biol.* **177**, 267–272 (2012).
133. Y. Liu and B. Levine, "Autosis and autophagic cell death: the dark side of autophagy," *Cell Death Differ.* **22**, 367–376 (2015).
134. S. T. Shibusaki and T. Yoshimori, "A current perspective of autophagosome biogenesis," *Cell Res.* **24**, 58–68 (2014).
135. D. Raoult, S. Audic, C. Robert, C. Abergel, P. Renesto, H. Ogata, B. La Scola, M. Suzan, and J.-M. Claverie, "The 1.2-megabase genome sequence of mimivirus," *Science* **306**, 1344–1350 (2004).
136. C. Abergel, M. Legendre, and J. M. Claverie, "The rapidly expanding universe of giant viruses: mimivirus, pandoravirus, pithovirus and mollivirus," *FEMS Microbiol. Rev.* **39**, 779–796 (2015).
137. M. Kördel, M. Svenda, H. K. N. Reddy, E. Fogelqvist, B. Hamawandi, M. S. Toprak, H. M. Hertz, and J. A. Sellberg, "Quantitative bioconversion in giant DNA virus infection," *Sci. Reports* (submitted for publication).
138. E. M. Mace, P. Dongre, H. T. Hsu, P. Sinha, A. M. James, S. S. Mann, L. R. Forbes, L. B. Watkin, and J. S. Orange, "Cell biological steps and checkpoints in accessing NK cell cytotoxicity," *Immunol. Cell Biol.* **92**, 245–255 (2014).
139. J. S. Orange, "Formation and function of the lytic NK-cell immunological synapse," *Nat. Rev. Immunol.* **8**, 713–725 (2008).
140. V. Weinhardt, J.-H. Chen, A. Ekman, G. McDermott, M. A. Le Gros, and C. Larabell, "Imaging cell morphology and physiology using x-rays," *Biochem. Soc. Trans.* **47**, 489–508 (2019).